Fastest spinning millisecond pulsars: indicators for quark matter in neutron stars?

Christoph Gärtlein,[1, 2, 3, *] Violetta Sagun,[2, †] Oleksii Ivanytskyi,[4, ‡] David Blaschke,[3, 5, 6, §] and Ilidio Lopes[1, ¶]

[1] *Centro de Astrofísica e Gravitação - CENTRA,*
Departamento de Física, Instituto Superior Técnico - IST,
Universidade de Lisboa - UL, Av. Rovisco Pais 1, 1049-001 Lisboa, Portugal
[2] *CFisUC, Department of Physics, University of Coimbra, 3004-516 Coimbra, Portugal*
[3] *Institute of Theoretical Physics, University of Wroclaw, 50-204 Wroclaw, Poland*
[4] *Incubator of Scientific Excellence—Centre for Simulations of Superdense Fluids,*
University of Wrocław, 50-204, Wroclaw, Poland
[5] *Helmholtz-Zentrum Dresden-Rossendorf (HZDR),*
Bautzner Landstrasse 400, 01328 Dresden, Germany
[6] *Center for Advanced Systems Understanding (CASUS), Untermarkt 20, 02826 Görlitz, Germany*
(Dated: December 11, 2024)

We study rotating hybrid stars, with a particular emphasis on the effect of a deconfinement phase transition on their properties at high spin. Our analysis is based on a hybrid equation of state with a phase transition from hypernuclear matter to color-superconducting quark matter, where both phases are described within a relativistic density functional approach. By varying the vector meson and diquark couplings in the quark matter phase, we obtain different hybrid star sequences with varying extension of the quark matter core, ensuring consistency with astrophysical constraints from mass, radius and tidal deformability measurements. As a result, we demonstrate the impact of an increasing rotational frequency on the maximum gravitational mass, the central energy density of compact stars, the appearance of the quasi-radial oscillations and non-axisymmetric instabilities. We demonstrate that for the most favorable parameter sets with a strong vector coupling, hybrid star configurations with color superconducting quark matter core can describe the fastest spinning and heaviest galactic neutron star J0952-0607, while it is out of reach for the purely hadronic hypernuclear star configuration.

We also revise the previously proposed empirical relation between the Kepler frequency, gravitational mass, and radius of non-rotating neutron stars, obtained based on the assumption that all neutron stars, up to the heaviest, are hadronic. We show how the phase transition to quark matter alters this relation and, consequently, the constraints on the dense matter equation of state. Our findings reveal that incorporating the hybrid equation of state has significant implications for the constraints on the properties of strongly interacting matter and neutron stars, placing the upper limit on $R_{1.4} \leq 14.90$ km (considering the 716 Hz frequency limit from J1748+2446ad) and $R_{1.4} \leq 11.90$ km (for 1000 Hz).

I.   INTRODUCTION

The most rapidly rotating neutron stars (NSs) are known as millisecond pulsars (MSPs) due to their millisecond-range rotation periods. In comparison, most pulsars are observed with a spin period in the 0.1 to 10-second range. MSPs are formed by the accretion-induced spin-up of the old NS in a close binary system. In the low-mass X-ray binary, the angular momentum transfer from the companion star onto the NS with infalling matter causes a "recycling" spin-up [1]. This process leads to the formation of such unique objects as MSPs, characterized by the extreme rotation frequency, remarkable rotational stability, high age ($\sim 10^9$ yr), and low magnetic fields ($\sim 10^{8-9}$ G) [2, 3].

Therefore, MSPs attract much attention as the unprecedented laboratory to test fundamental physics.

Thus, high-precision pulse measurements in compact binaries allow unique tests of the theories of gravity with the double-pulsar system J0737-3039 [4] and obtaining the spin-orbit coupling, which allows extracting the moment of inertia [5, 6]. The latter, together with the simultaneous measurements of pulsar mass and radius with the NICER telescope, aim to constrain the dense matter equation of state (EoS) and probe the interior composition of NSs [7]. MSPs in binary systems, e.g. "spider" pulsar binaries, are also targets for mass determination [8, 9].

Although theoretical models of NSs allow much higher spin rotation rates above 1 kHz, the fastest known pulsar, PSR J1748-2446ad, has a spin period of 1.4 ms (716 Hz) [10]. This fact raised a lot of discussions regarding whether the observed limit of $\sim$700 Hz corresponds to the spin frequency cutoff related to the Kepler (mass-shedding) limit above which matter becomes unbound [11], it is related to the binary system evolution [12] or the result of the deconfinement phase transition in the NS core causing either the change of the frequency distribution [13] or the rotational frequency cutoff [14].

* christoph.gartlein@tecnico.ulisboa.pt
† violetta.sagun@uc.pt
‡ oleksii.ivanytskyi@uwr.edu.pl
§ david.blaschke@uwr.edu.pl
¶ ilidio.lopes@tecnico.ulisboa.pt

On the other hand, modelling the rapidly rotating MSPs involves advanced numerical methods compared to the slow-rotating NSs, which require solving additional coupled differential equations. Rotation causes an NS to deform into an oblate spheroid, resulting in a larger equatorial radius and an increased gravitational mass compared to a non-rotating NS, which is related to an increase of the centrifugal force (see illustration of star's deformation in Fig. 1). As rotation affects the star's compactness, it alters the matter composition and, consequently, its dynamical properties, e.g. moment of inertia [15–20]. Another example of such rotation-driven changes is the thermal evolution of NSs [21, 22]. An increase in the central density can trigger new processes, such as the direct Urca process, which is forbidden at lower central densities but may become active as the star spins down, leading to its rapid cooling [21, 23]. As the

static case $\Omega = 6$ **kHz** **Kepler frequency**

FIG. 1. Modification of the NS shape due to rotation.

maximum rotational frequency and star's properties are determined by the EoS of cold dense strongly interacting matter, it is necessary to reproduce the observational data together with realistic models that satisfy existing constraints and account for the possibility of the existence of an exotic phase in the NS core, e.g. hyperons, phase transition to quark matter. Thus, in this work, we explore the effect of rotation on the hybrid star properties characterized by the different quark matter properties and onset density of the phase transition. This study is especially important due to the discussed in the literature rotationally induced phase transition to the quark matter in the NS core [24, 25]. As a star gradually spins down over time, the increasing compression of matter could trigger a phase transition to deconfined quarks at the corresponding density.

While the rapidly rotating hybrid stars have been studied in several papers in the past, e.g. Ippolito *et al.* [26], Dhiman *et al.* [27], Ayvazyan *et al.* [28], Bhattacharyya *et al.* [29], Largani *et al.* [30], this topic got new insights due to the recent observations of NICER, heavy pulsars, and detection of many new MSPs with the ongoing radio surveys. Thus, the study of the fast-spinning NSs and their maximum spin frequency (i.e., the Kepler frequency) [31] is especially important after the three recent NICER measurements, PSR J0030+0451 [32, 33], PSR J0740+6620 [34, 35] and PSR J0437-4715 [36], together with the stringent maximum mass limit [8, 9, 37].

In the present work, the quark phase is described by the effective model that captures the aspects of confine-

ment and color superconductivity, as well as perturbative QCD corrections [38]. In Gärtlein *et al.* [39] the fit of the utilized model by the Alford-Braby-Paris-Reddy (ABPR) parameterization [40] is presented, providing a simple functional relation between the key parameters of the EoS and the microscopic parameters of the initial Lagrangian.

This article presents a thorough analysis of the impact of rotation on hybrid star properties and stability against quasi-radial and non-axisymmetric oscillations utilizing astrophysical and gravitational wave (GW) constraints on the cold, dense matter EoS, together with the fastest MSP measurements. It allows us to revise the previously found empirical formulas relating the mass and radius of the star with the Kepler frequency. We demonstrate how the first-order phase transition in the hybrid star interior alters the previously found relations.

The article is organized as follows. In Sec. II, we describe the hadronic and quark EoSs and how we construct the hybrid stars. Sec. III presents the theoretical framework to model uniformly rotating stars and the impact of rotation on the star's properties. Sec. IV discusses the Kepler frequency and empirical relations. In Sec. V, we show our findings for the effect of rotation on the stability of hybrid stars and constraints on their interior composition. Finally, Sec. VI summarizes the results. Throughout the article, we use the natural unit system in which $\hbar = c = G = 1$.

II. HYBRID STARS

A. EoS of hadronic matter

The hadronic matter is described within the relativistic density functional DD2npY-T EoS [41] that includes nucleonic and hyperonic degrees of freedom. The DD2npY-T EoS satisfies the maximum mass constraint [8, 9, 37], the LIGO-Virgo tidal deformability measurements of GW170817 [42] and GW190425 [43] binary NS mergers and NICER results [32–36].

Below the saturation density, the DD2npY-T model is supplemented by the generalized relativistic density functional (RDF) EoS for the crust [44]. It incorporates nuclei in a body-centred cubic lattice with a uniform background of electrons supplemented with a neutron gas above the neutron drip line. The transition between the generalized RDF and DD2npY-T models is consistently described within the unified approach.

B. EoS of quark matter

Quark matter is modeled based on the confining RDF approach with color superconductivity [38, 45]. The confining aspect is connected to the dynamical breaking of chiral symmetry, which, at small temperatures and densities, leads to large effective quark masses above 0.7

GeV and efficiently suppresses quark excitations. The approach is equivalent to a chiral quark model with medium-dependent couplings of the scalar and pseudo-scalar channels, which in the general case are different due to the breaking of chiral symmetry but coincide when the chiral symmetry gets restored [38]. The medium dependence of the vector and diquark couplings is adjusted in order to reach the conformal limit of quark matter [45]. Fitting the pion mass and decay constant, sigma meson mass and chiral condensate in vacuum fixes all the model parameters except the vector and diquark couplings (see Ref. [38] for details). The latter are parameterized in terms of their dimensionless ratios to the scalar coupling evaluated in the vacuum, i.e. η_V and η_D being the only free parameters of the model.

In this work, we use the ABPR parameterization of the RDF EoS, which was proposed in Ref. [39]

$$p = \frac{A_4 \mu^4}{2\pi^2} + \frac{\Delta^2 \mu^2}{\pi^2} - B. \tag{1}$$

The parameters A_4, Δ, and B in Eq. (1) are the effective number of degrees of freedom, pairing gap, and bag pressure. They are unambiguously defined by the dimensionless couplings η_V and η_D. The corresponding functional dependencies can be found in Appendix A.

The two-phase hybrid star EoS is constructed by matching its hadron and quark branches according to the Maxwell construction. The corresponding quark-hadron phase transition is of the first order. The energy density jumps across the phase boundary, and the properties of hybrid stars are fully determined by the dimensionless couplings η_V and η_D. Previous work [39] has already explored the roles of these parameters. The diquark coupling η_D governs the onset of the deconfinement phase transition, with only a minor impact on the maximum mass of hybrid stars. In contrast, variation of the vector coupling η_V affects the stiffness of the EoS and, therefore, the maximum mass of hybrid stars. In this work, we vary η_V and η_D in the range, where all the available astrophysical constraints are respected [39].

III. ROTATING NEUTRON STARS

A. Theoretical framework

For the rapidly rotating relativistic compact stars, we have to apply an appropriate framework. The starting point is an axisymmetric spacetime metric [46]

$$ds^2 = e^{2\nu}dt^2 - e^{2\psi}(d\phi - \omega dt)^2 - e^{2\lambda}(dr^2 + r^2 d\theta^2). \tag{2}$$

The metric functions ν, ψ, ω and λ only depend on r and θ. The choice, $e^\psi = r^2 \sin^2 \theta B^2(r, \theta) e^{-\nu}$ shows the difference with respect to the static NS metric. For rotating stars, the centrifugal force causes its flattering, resulting in a larger equatorial radius and an increased

gravitational mass compared to a non-rotating NS. More-over, the so-called *dragging* of the local inertial frame due to the gravitational field of the source is a purely rela-tivistic effect [47, 48]. The spacetime fabric around the rotating gravitational object is distorted and the orbit of nearby test particles will start to precess. It is often called a "gravitomagnetic" effect due to the analogue of this phenomenon in electromagnetism [49]. In order to account for the dragging of the inertial frames, one intro-duces the Zero-Angular-Momentum-Observers (ZAMO) frame [50]. From the view of an observer at rest at infi-nity, observers in a local ZAMO frame would move with the angular velocity ω (see Eq. (2)).

The considered axisymmetric metric appears under the following conditions: (i) there are two Killing vector fields, t^α as usual, and ϕ^α due to axial symmetry; (ii) asymptotically flat spacetime.

In addition, we approximate the NS interior as a per-fect fluid:

$$T^{\alpha\beta} = (\varepsilon + p)u^\alpha u^\beta + pg^{\alpha\beta} , \tag{3}$$

where ε and p denote the energy density and pressure of the fluid, respectively, while u^α denotes the fluid 4-velocity vector.

Taking advantage of the symmetries of our system, the 4-velocity can be written in terms of the two Killing vec-tors:

$$u^\alpha = \frac{e^{-\nu}}{\sqrt{1 - v^2}}(t^\alpha + \Omega\phi^\alpha) , \tag{4}$$

where the fluid 3-velocity vector v with respect to the local ZAMO frame and $\Omega = \frac{d\phi}{dt}$, the angular velocity measured by an observer at rest at infinity were intro-duced [46]. The two quantities are related as

$$v = (\Omega - \omega)e^{\psi - \nu} . \tag{5}$$

To derive the corresponding field equations, we need to solve the Einstein equations. In detail, the conservation of the energy-momentum tensor in Eq. (3) including the metric components of Eq. (2) and the Killing vectors of Eq. (4) needs to be solved. The hydrostatic equilibrium equation will then read

$$p_{,i} = -(\varepsilon + p)\left[\nu_{,i} + \frac{1}{1 - v^2}\left(vv_{,i} + v^2 \frac{\Omega_{,i}}{\Omega - \omega}\right)\right]. \tag{6}$$

In the limit of non-rotating NSs, the functions ω and Ω should both vanish as none of the observers will observe any rotation. For $v \to 0$, Eq. (6) equals to

$$p_{,i} = -(\varepsilon + p)\nu_{,i}, \tag{7}$$

as in the case of deriving the Tolman-Oppenheimer-Volkoff (TOV) equations [51, 52] for static gravitational objects.

These equations for the static objects read [51, 52]

$$\frac{dp}{dr} = -(\varepsilon + p)\frac{m + 4\pi pr^3}{r^2 - 2rm}, \tag{8}$$

$$\frac{dm}{dr} = 4\pi r^2 \varepsilon. \tag{9}$$

The differential equations in the rotating as well as in the static cases are solved by applying the same boundary conditions: (i) $m(0) = 0$, $p(0) = p_c$, with p_c being the pressure in the center of a star; (ii) pressure and energy density vanish at the surface of the star $r = R$. By fixing the value of the central pressure and varying it up to $p(R) = 0$ we are able to numerically obtain the radius R and enclosed gravitational mass $m(R) = M$ of the NS. For each considered value of the angular velocity, the $M - R$ curve is obtained by utilizing the publicly available RNS[1] code that calculates the properties of rapidly rotating relativistic compact stars [53]. We consider uniformly rotating stars described by the hybrid EoS with different onsets of the deconfinement phase transition and quark matter properties. Fig. 2 shows a set of $M - R$ curves for static (solid curves) and rotating hybrid stars with the Kepler frequency (dashed curves). Following Gärtlein *et al.* [39] to account for uncertainties in the dense matter EoS we utilize a set of six hybrid star configurations with different properties. The color represents the unique value of the diquark coupling defining the onset of the phase transition, while the value of the vector coupling η_V is fixed at 0.30. The intriguing feature of the utilized RDF model is that it could describe hybrid stars with a wide range of properties, including the different onset and strength of the deconfinement phase transition. The set also includes hybrid stars with an early deconfinement phase transition. Table I lists the considered values of the vector and diquark couplings as well as the corresponding onset mass of the deconfinement phase transition and maximum gravitational mass for static configurations presented in Fig. 2. All these

η_V	η_D	$n_{\rm onset}$ [fm^{-3}]	$M_{\rm onset}^{\rm TOV}$ [$M_\odot$]	$M_{\rm max}^{\rm TOV}$ [$M_\odot$]	$M_{\rm onset}^{K}$ [$M_\odot$]	$M_{\rm max}^{K}$ [$M_\odot$]
0.3	0.733	0.3715	1.488	2.114	1.927	2.539
	0.737	0.3311	1.292	2.112	1.662	2.534
	0.743	0.2951	1.053	2.116	1.319	2.540
	0.750	0.2455	0.686	2.133	0.843	2.578
	0.755	0.2138	0.488	2.148	0.573	2.621
	0.760	0.1778	0.295	2.167	0.322	2.688
0.452	0.775	0.3467	1.347	2.403	1.692	2.935
	0.780	0.2455	0.666	2.414	0.739	2.965

TABLE I. Parameters of the considered set of hybrid EoSs depicted used throughout this paper. $M_{\rm onset}$ and $n_{\rm onset}$ are the mass and baryon density of the deconfinement phase transition onset. The superscripts TOV and K represent the static and Kepler limits.

configurations are characterized by a different size of the quark core, the strength of the first-order phase transition (jump in the energy density at the phase transition), and the speed of sound values in the quark phase (for more details see [39]). As can be seen in Fig. 2, due to the centrifugal force, the rotating configurations (see the

dashed curves of the corresponding color) are more massive in comparison to non-rotating counterparts, whereas the main features of static NSs, e.g. the onset density of the deconfinement phase transition, the special point (the point in which a set of $M - R$ curves intersect [54]), etc., are preserved.
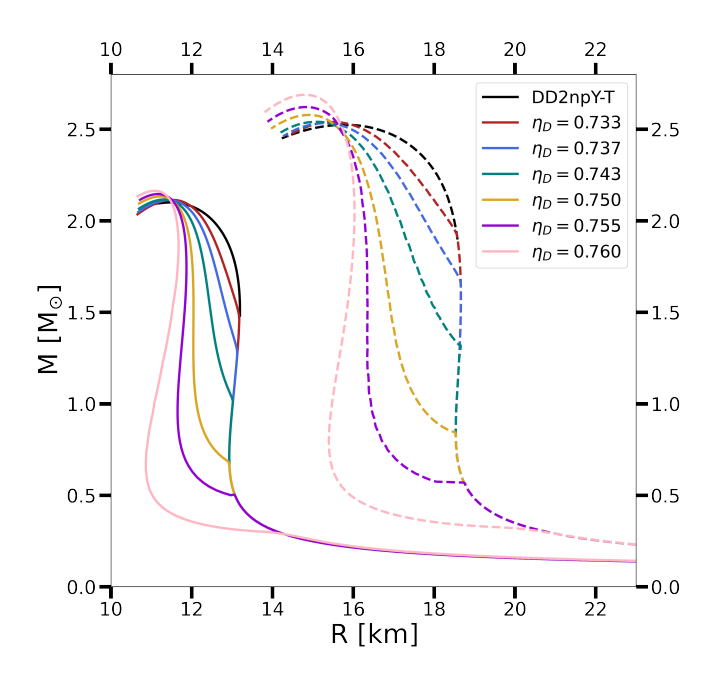

FIG. 2. Mass-radius diagram for a set of static (solid curves) and rotating stars with the Kepler frequency (dashed curves). The black and color curves depict the baryonic DD2npY-T EoS as well as hybrid stars for the fixed vector coupling $\eta_V = 0.30$ and different values of the diquark coupling η_D, respectively. The radius corresponds to the equatorial radius. The allowed configurations for hybrid stars are located between the solid and dashed curves of the same color.

As shown in Refs. [55–57], non-rotating stars remain stable along the M-R curve up to the maximum gravitational mass, where the frequency of the fundamental eigenmode becomes zero. Beyond this critical value, the star becomes unstable, and the frequency of the radial oscillation mode turns imaginary. At such high densities, the fundamental mode of infinitesimal radial perturbations becomes unstable, leading to the collapse of the star into a black hole, which corresponds to the instability criterion $\partial M/\partial \varepsilon_c < 0$.

Fig. 2 indicates the stability region for rotating NSs. Thus, hybrid stars with the early deconfinement phase transition are stable between the solid and dashed light pink curves, which correspond to the configurations of non-rotating and the ones with the Kepler frequency, respectively. The region between the solid and dashed dark red curves represents the sequence of stars with the late phase transition.

B. Impact of rotation on compact star structure

Oblateness. The oblateness or ellipticity of a star is defined as

$$e = \sqrt{1 - (R_{\mathrm{p}}/R_{\mathrm{eq}})^2}, \qquad (10)$$

where R_{p} and R_{eq} are the polar and equatorial radii, respectively. Assuming that for not too large ellipticities holds $R_{\mathrm{p,eq}} = R \mp \Delta R$, then follows that

$$e = 2\sqrt{R_{\mathrm{eq}}/R - 1}. \qquad (11)$$

As it is schematically shown in Fig. 1 the increase of the spin frequency causes a deviation from the spherically symmetric configuration that reaches its maximum at the Kepler frequency. Let us assume that the deformation of the star, i.e. its oblateness, is proportional to the ratio of rotational, T, and gravitational, W, energy, which for a homogeneous Newtonian star is $T/W = (\Omega/\Omega_0)^2$, where $\Omega_0^2 = 4\pi\rho(0)$ and $\rho(0)$ is the mass density at the center of the star. This ratio is the small expansion parameter in the perturbative treatment of general relativistic rotating star configurations [58–60]. Then according to Hooke's principle, the deformation should be proportional to the ratio $\Delta R/R = a(\Omega/\Omega_K)^2$, where we used the proportionality between Ω_0 and the Kepler frequency $\Omega_K = 2\pi f_K$ (for its definition, see below) and introduced the coefficient a for the elasticity (deformability) of matter. The equatorial radius in the lowest order is then $R_{\mathrm{eq}} = R(1 + a(\Omega/\Omega_K)^2)$ so that from Eq. (11) follows the linear response of the oblateness to the rotation frequency (angular velocity)

$$e = 2\sqrt{a}\,\Omega/\Omega_K. \qquad (12)$$

Fig. 3 shows the relation between the oblateness and angular velocity (upper panel) as well as the normalized angular velocity for the Kepler velocity (lower panel) for a star of the fixed rest mass $M = 1.5\ M_\odot$ ($M_{\mathrm{grav}} \approx 1.4\ M_\odot$). Note that the rest mass is equal to the baryon mass. The curves in Fig. 3 are obtained for $\eta_V = 0.3$ and different values of the diquark coupling $\eta_D = 0.733 - 0.760$. On the upper panel, the behavior of all curves is strictly linear and universal with $2\sqrt{a} \approx 0.772$ (see the dashed black lines), even for angular velocities as close as 95% of the mass-shedding velocity. The deviation in oblateness is related to the stiffness of the quark matter defined by the value of the diquark coupling η_D. The lower panels of Fig. 3 show the absolute and relative deviations of the fitting function from the data. The latter does not exceed 6%. The critical diquark coupling for which a star of this mass shall undergo a deconfinement transition is $\eta_D = 0.737$. Remarkably, we do not observe a significant change in the slope at the deconfinement phase transition (see the dashed vertical lines on the lower panel of Fig. 3 depicting the onset of the phase transition for $\eta_D = 0.736$ and $\eta_D = 0.737$) that

results in a good agreement with $2\sqrt{a} \approx 0.772$ value for all curves.

Our study confirms the results of [61], which showed that the changes in polar and equatorial radii are symmetric, with the polar radius shrinking at the same rate that the equatorial radius expands.

In addition, the commonly used quantity as a star's compactness, $\mathcal{C} = M/R$, which is defined for a static star, loses its meaning for rapidly-spinning NSs. This definition does not apply to rapidly rotating compact stars, especially those near the Kepler frequency. In principle, the compactness can be derived from the g_{00} component of the corresponding metric. In the static case, this corresponds to $g_{00} = -(1 - 2\mathcal{C})$. However, when considering rotation, the loss of symmetries significantly complicates the situation. As discussed by Hartle [62], Hartle and Thorne [63], even the metric for a slowly rotating (approximately spherical) star is non-trivial. In the lowest order of the multipole expansion, the g_{00} component of the metric is given by

$$g_{00} = -\left(1 - 2C\right)\left(1 - \frac{2\delta M}{r - 2M} + \frac{2J^2}{r^3(r - 2M)} + ...\right) \quad (13)$$

where (...) include even higher orders, δM denotes the change of mass due to rotation and J is the corresponding angular momentum. Consequently, the compactness $\mathcal{C}$ for rotating stars needs a redefinition.

Matter distribution. As described in Section II the two-phase hybrid star EoS is constructed by matching its hadron and quark EoSs with the Maxwell construction. While the low-mass stars consist of hadronic matter, increasing the central energy density leads to the onset of the deconfinement phase transition. In Fig. 4, the jump in energy density (horizontal dotted line) shows the transition region from hadronic to quark matter. No stable configurations are located along the horizontal dotted lines. Stars with a central energy density above the onset are hybrid stars with a quark core. As expected, an increasing diquark coupling triggers a much earlier onset of the deconfinement phase transition. We see that stars rotating at the Kepler frequency (dashed curves in Fig. 4) show a similar structure to the non-rotating configurations (solid curves). The effect of rotation becomes more pronounced the later the phase transition occurs. Consequently, a higher value of η_D leads to phase transitions at lower masses, and under rotation, the onset of these transitions shifts towards higher masses. In general, the more massive the object, the greater the shift towards higher masses. Therefore, an earlier phase transition will occur in low-mass stars, which can only remain stable under slow rotation. As a result, the shift due to the fastest possible spin is insignificant. In the case of $\eta_D = 0.733$, we clearly observe the impact of rapid rotation: the onset of the deconfinement phase transition shifts to higher masses, M_{onset}, for the same central energy density, and the maximum mass increases by approximately $\approx 20\%$.
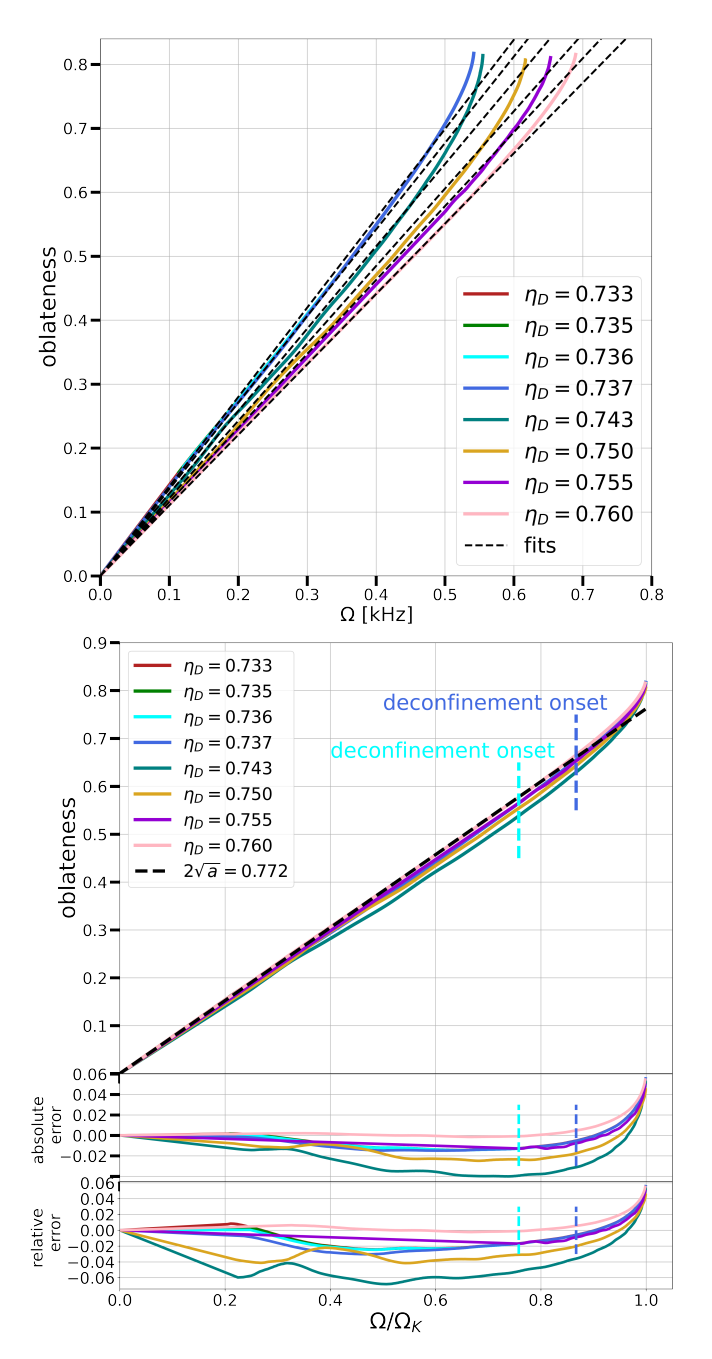
FIG. 3. **Upper panel:** The oblateness/eccentricity e as a function of the angular velocity for the fixed value of the vector coupling $\eta_V = 0.3$ and varying diquark coupling η_D. **Lower panel:** The oblateness/eccentricity e as a function of the normalized angular velocity Ω to the Kepler (mass-shedding) velocity Ω_K. The vertical dashed light and dark blue lines show the frequency of the phase transition onset at the corresponding solid curves. The black dashed line shows the optimal fit for $2\sqrt{a}$. The absolute error according to this fit is shown below. On both panels, the curves corresponding to the lowest η_D values lay behind the blue curve as they coincide up to the high mass. The colors are the same as in Fig. 2.
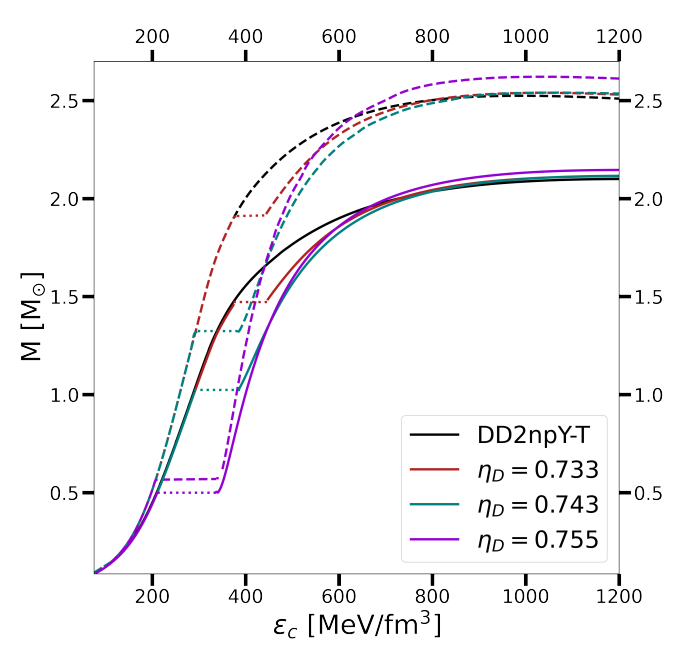

FIG. 4. The gravitational mass as a function of the central energy density for a set of static (solid curves) and rotating with the Kepler frequency (dashed curves) hybrid stars for the fixed vector coupling $\eta_V = 0.3$ and different η_D values listed in the legend (color curves). The dotted plateaus correspond to the first-order phase transition region. The solid black curve represents the hadronic stars modelled within the DD2npY-T EoS.

IV. THE KEPLER FREQUENCY

The Kepler frequency plays an important role in understanding the interior composition of compact stars [64]. Any rotation at a faster speed will result in mass-shedding from the star's equator. Shapiro *et al.* [65] proposed the relativistic Roche model, for which the equality of the Kepler frequency with that of a particle orbiting at $r = R_K$ in the Schwarzschild spacetime around a point of mass M at $r = 0$ strictly holds [60, 66]

$$f_K^{\mathrm{Roche}} = \frac{1}{2\pi}\left(\frac{M}{R_K^3}\right)^{1/2}, \qquad (14)$$

where R_K and M are the circumferential equatorial radius R_{eq} and the gravitational mass of the Keplerian configuration.

A slightly different empirical relation can be written down between the Kepler frequency f_K, gravitational mass M of the Keplerian configuration, and radius R of the non-rotating star

$$f_K = C\left(\frac{M}{M_\odot}\right)^{1/2}\left(\frac{R}{10\,\mathrm{km}}\right)^{-3/2}. \qquad (15)$$

Relating two empirical formulas, the factor C for the

Roche model is equal to

$$C^{\text{Roche}} = \frac{1}{2\pi}\left(\frac{2}{3}\right)^{3/2}\left(\frac{M_\odot}{(10\,\text{km})^3}\right)^{1/2} \quad (16)$$
$$= 1.007\,\text{kHz}.$$

For realistic EoS, the factor C is obtained by numerically calculating the Kepler frequency and comparing it with the empirical formula (15). It is defined as

$$C(M) = f_0\left(\frac{R(M)}{R_K(M)}\right)^{3/2}, \quad (17)$$

where $f_0 = (3/2)^{3/2}C^{\text{Roche}} = 1.8335\,\text{kHz}$. It was determined to be 1.04 kHz [67] and further revised by Haensel *et al.* [66] who found $C{=}1.08$ kHz for soft hadronic EoSs (e.g., APR, WFF, FPS) and $C{=}1.15$ kHz for strange quark stars. An alternative polynomial function relating the Keplerian and static star properties is proposed by Riahi *et al.* [68]. One could, therefore, think of suggesting the value of C as an indicator characterizing the star's interior. An empirical formula Eq. (15) for the Kepler frequency is essential for constraining the EoS of strongly interacting matter with pulsar observations. Avoiding the computationally demanding numerical calculations Eq. (15) provides a simple and universal relation between the quantities.

While the values $C{=}1.08$ kHz and $C{=}1.15$ kHz are obtained for one-phase stars, i.e. hadronic and quark stars [66], the deconfinement phase transition in the NS interior alters the obtained value of the factor C. Moreover, accommodation of the phase transition onset at various densities poses a complication.

To obtain the behavior of $C(M)$ for the considered set of hybrid stars (see Table I), the masses of Keplerian M^K and static M^{TOV} configurations are matched following the relation of Breu and Rezzolla [69] suggesting a factor $M^K = bM^{TOV}$, where $b = 1.204 \pm 0.002$. However, we found that for each set of model parameters, b has slightly different values in the range $1.0 - 1.3$.

For most stars, the internal composition of both static and Keplerian configurations is the same, either hadronic or hybrid, resulting in similar values of C. However, within a narrow range of stellar masses, the two configurations differ, leading to a drop in $C(M)$ by approximately $80 - 100$ Hz. This behavior can be understood from the definition of $C(M)$ in Eq. (17). In this mass region, the static configuration is already significantly compactified due to the deconfinement transition, while the Keplerian configuration at the same mass remains in the hadronic phase with a larger radius. To avoid comparing hadronic stars with hybrid stars, the masses of static and rotating configurations are matched using a scaling factor $b = 1.0 - 1.3$.

Fig. 5 illustrates the behavior of C as a function of the gravitational mass of the Keplerian configuration M^K. We find the $C = 1.088$ kHz value to be a better fit for the stiff DD2npY-T EoS in comparison to the $C = 1.08$
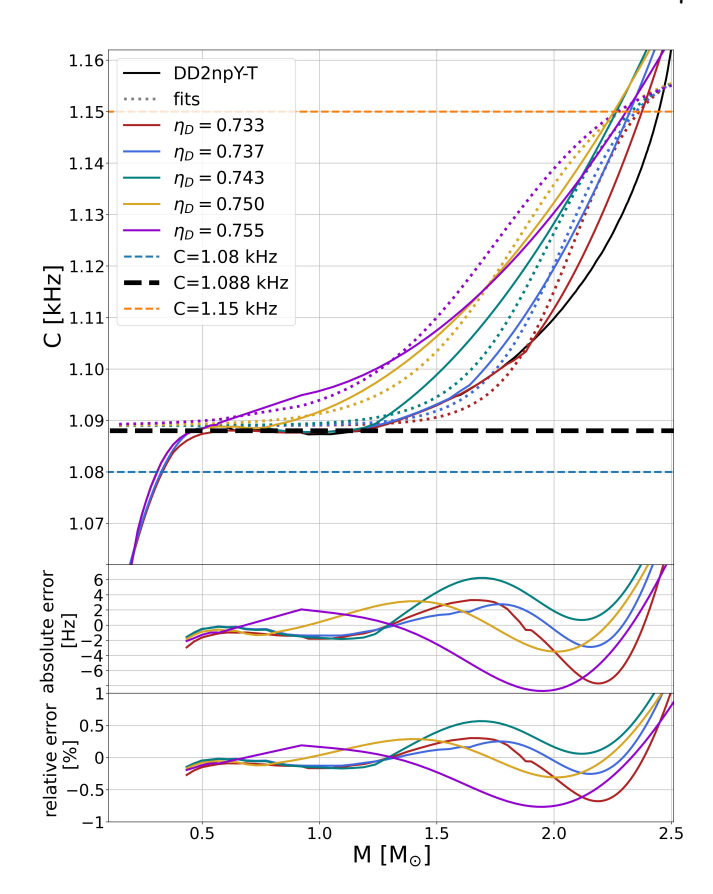

FIG. 5. Behavior of the empirical factor C as a function of the gravitational mass M of the Keplerian configuration for a set of hybrid stars. The solid curves illustrate the data, whereas the dotted curves show the fit with different deconfinement onset with Eq. (18). The horizontal dashed lines indicate C=1.08 kHz (blue), C=1.088 kHz (black) obtained for hadronic EoSs, and C=1.15 kHz (orange) obtained for quark EoSs. The lower panels indicate the absolute and relative error of the fit.

kHz value obtained for a set of soft hadronic EoS [66]. In the range between 0.5 $M_\odot$ and the onset of quarks, the value of C remains constant at 1.088 kHz, as shown by the black dashed line. The subsequent deviation from this constant value is associated with the deconfinement phase transition. For hybrid stars, C increases after the phase transition, reaching a maximum of $C = 1.15 - 1.16$ kHz. This result confirms that the hybrid EoS successfully reproduces the two limiting cases of hadronic and quark EoSs while incorporating the transition between them.

To account for different quark matter properties and the onset density of the deconfinement phase transition, we derived the parametrization of C as a function of the onset mass M_{onset} and gravitational mass at the Kepler frequency M^K

$$C = C_{\text{had}} + \frac{\delta C}{1 + 5e^{(D(M_{\text{onset}}) - E(M_{\text{onset}})M^K)}}. \quad (18)$$

Here $\delta\text{C} = 0.072$ kHz is defined as the difference be-

tween the value of C in the quark and hadron limits $\delta C = C_{\text{quark}} - C_{\text{had}} = 1.16$ kHz $- 1.088$ kHz. The obtained formula (18) corresponds to the logistic function with the inflection point equal to $E(M_{\text{onset}}) \cdot M^K$, where the dimensionless parameter $E(M_{\text{onset}}) = 3M_{\text{onset}} + 2$. The dimensionless function D is equal to $D(M_{\text{onset}}) = 7.5M_{\text{onset}} + 0.7$.

This simple formula provides a good description of the C factor in a wide range of the hybrid star properties and the onset of the phase transition with the maximal deviations of the order of ± 8 Hz and the relative error below 1% (see the bottom part of Fig. 5). The obtained fit is depicted as the dotted curves in Fig. 5. The values of the onset mass were taken from Table I. Note that the fit was performed between 0.5 $M_\odot$ and the maximum mass.

The obtained parameterization reproduces two limits, i.e. hadronic stars with $C_{\text{had}} = 1.088$ kHz and quark stars with $C_{\text{quark}} = 1.16$ kHz. The universal parameterization of C considering the onset of the deconfinement phase transition at different densities is a useful tool to account for the general relativistic effects in the description of rapidly rotating stars with a different interior composition.

The fastest spinning pulsar, PSR J1748-2446ad, with a spin frequency of 716 Hz [10], is used to put a limit on the NS properties and dense matter EoS. The lower limit on the M-R relation obtained by Haensel *et al.* [66] for a set of hadronic EoSs is depicted with the gray dashed curve in Fig. 6. The gray-shaded area below shows an excluded region for NSs. On the other hand, the limits coming from quark EoSs with $C = 1.15$ kHz and the hybrid EoS with the early deconfinement phase transition ($\eta_V = 0.30$, $\eta_D = 0.755$) are depicted by the black and orange dashed curves, respectively. As you can see in Fig. 6 hadronic EoSs provide a more stringent constraint on the mass and radius of low-mass NSs, while the hybrid EoS does not show a big difference from the former one. This insignificant deviation of the orange curve from the gray one could easily be understood from the behavior of the C factor in Fig. 5. Thus, in the middle-mass range, the deviation of C for hybrid EoS from the hadronic $C_{\text{had}} = 1.088$ kHz line does not exceed 20 Hz, while the difference becomes significant for higher masses. Therefore, detection of a pulsar with a 1000 Hz spinning frequency could lead to a much more stringent constraint on the compact star properties. The dash-dotted gray, black, and orange curves illustrate the lower bounds for the hadronic, quark, and hybrid EoS, respectively.

The inclusion of the hybrid EoS in the analysis of PSR J1748-2446ad resulted in a revised upper limit on the radius of a 1.4 solar mass NS. The limit extends from $R_{1.4} \leq 14.78$ km (for the hadronic EoSs) to $R_{1.4} \leq 14.90$ km (for the hybrid EoS with the early deconfinement phase transition $\eta_V = 0.30$, $\eta_D = 0.755$). The detection of an even faster-rotating pulsar, e.g., with a spin frequency of 1000 Hz, would impose even tighter con-

straints on the properties of strongly interacting matter. It would also alter the upper limit from $R_{1.4} \leq 11.86$ km (hadronic EoS) to $R_{1.4} \leq 11.90$ km (hybrid EoS), providing significant insights into the EoS of dense matter.
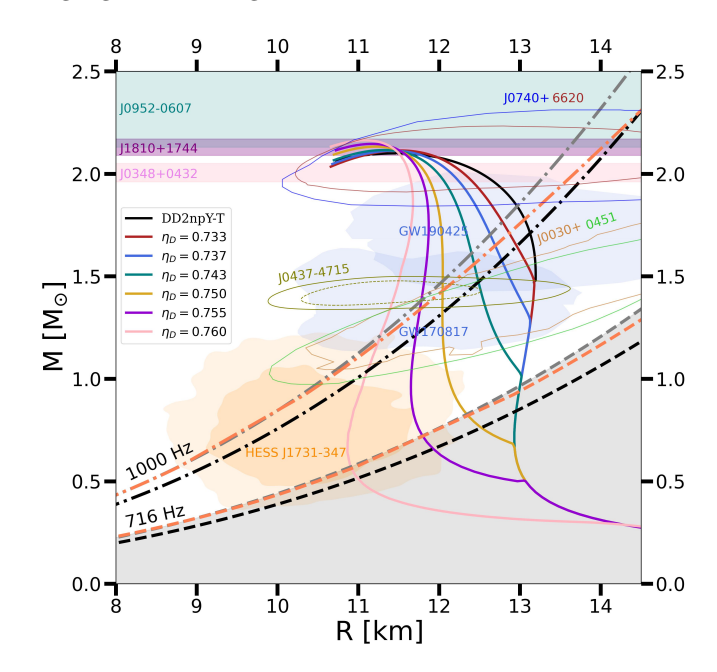

FIG. 6. Mass-radius relations for a set of static hybrid stars for the fixed vector coupling $\eta_V = 0.30$ and different values of the diquark coupling η_D as well as baryonic stars modeled within the DD2npY-T EoS (black curve). The teal, purple, and violet bands represent the 1σ constraints on the mass of PSR J0952-0607 [9], PSR J1810+1744 [8], and PSR J0348+0432 [37]. The NICER measurement of PSR J0030+0451 [32, 33] is depicted with the light brown and lime green contours, while blue and brown contours represent the PSR J0740+6620 measurement [34, 35]. The olive solid (95% CL) and dashed (68% CL) contours represent the newly reported NICER measurement of PSR J0437-4715 [36]. LIGO-Virgo detections of GW170817 [42] and GW190425 [43] binary NS mergers are shown in light blue. The 1σ and 2σ contours of HESS J1731-347 [70] are plotted in dark and light orange, respectively. The gray dashed curve and shaded gray region below are the lower boundary of the M-R relation obtained for the currently fastest spinning pulsar PSR J1748-2446ad [10] considering the value $C = 1.08$ kHz found in [66]. The black and orange dashed curves depict the excluded region of the M-R diagram obtained for the quark EoS with $C = 1.15$ kHz and hybrid EoS with the early deconfinement phase transition ($\eta_D = 0.755$). The dash-dotted gray, black and orange curves illustrate the constraint coming from the detection of a pulsar with 1000 Hz spinning frequency considering the hadronic, quark and hybrid EoS, respectively.

V. RAPIDLY ROTATING HYBRID STARS

For a better comparison, we selected hybrid star configurations for four pairs of couplings, namely ($\eta_V = 0.3, \eta_D = 0.733$), ($\eta_V = 0.3, \eta_D = 0.743$), ($\eta_V =$

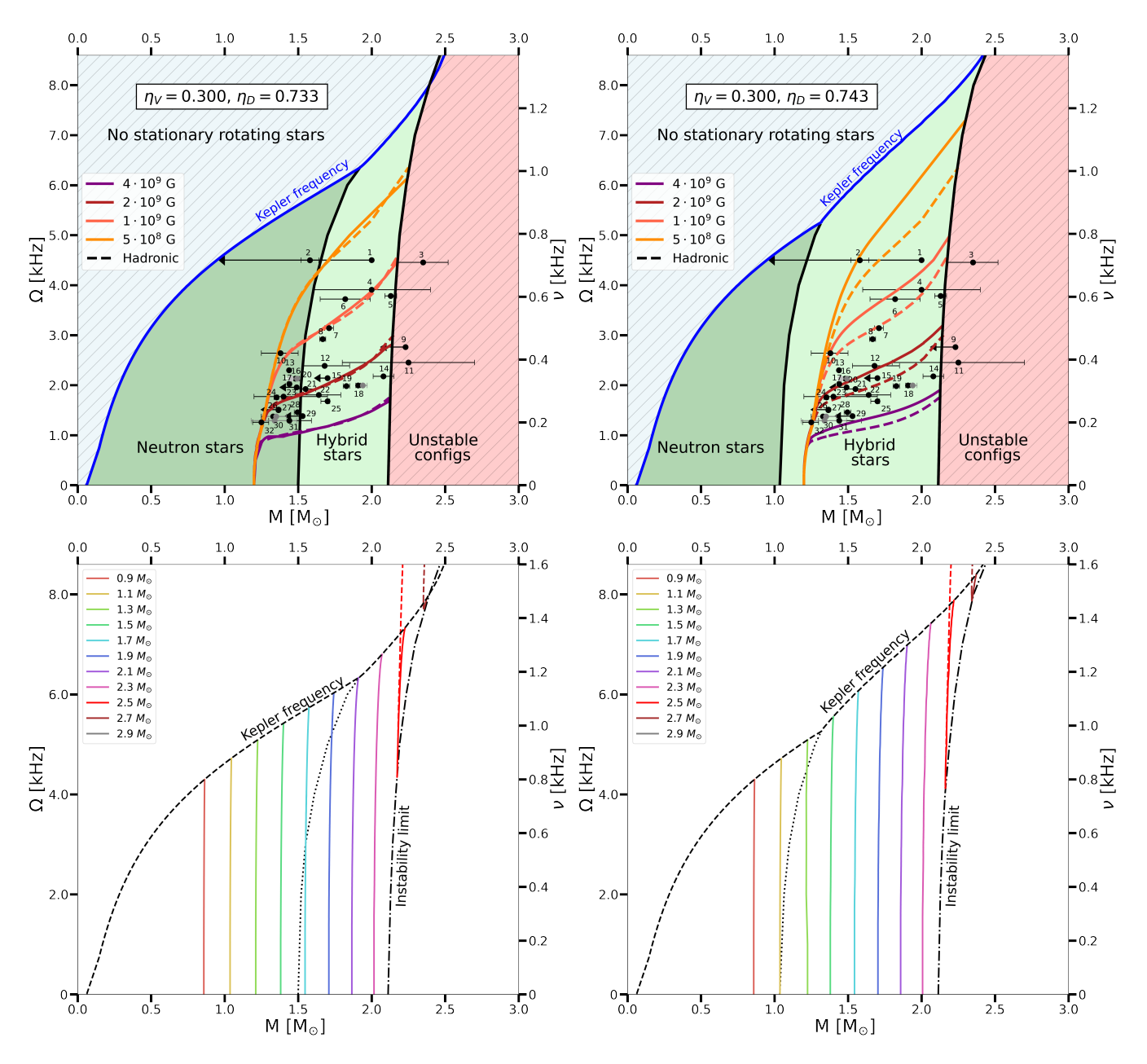FIG. 7. **Upper panel:** The angular velocity as a function of the gravitational mass of hybrid stars. The solid blue curve represents the Kepler frequency, above which lies the gray-shaded area where no stationary rotating stars can be found. Black solid curves mark the separation between NSs (dark green area), hybrid stars (light green area), and black holes (pink beige area of unstable configurations). The circles with 1σ confidence level error bars depict the measured mass and frequency of the fastest known MSPs with spin frequency f>200 Hz (the data are listed in Appendix B). The arrows, rather than error bars, represent the available upper limit on the mass estimate. Other independent mass measurements of the same object are depicted with gray dots. The color solid curves represent the evolution trajectories of the hybrid (solid) and hadronic (dashed) star of $1.2 M_\odot$ with the corresponding strength of the magnetic field. **Lower panel:** Evolutionary paths of non-accreting unmagnetized stars of the fixed constant rest mass depicted in different colors. The x-axis shows the gravitational mass. The dotted curve indicates the NS-hybrid star separation, similar to the upper panel. The results are obtained for the fixed value of the vector coupling $\eta_V = 0.3$ and different values of the diquark coupling $\eta_D = 0.733$ (left panels) and $\eta_D = 0.743$ (right panels).

$0.452, \eta_D = 0.775)$ and $(\eta_V = 0.452, \eta_D = 0.780)$. This choice is motivated by the correlation between the diquark coupling value and the onset mass of the deconfinement phase transition found in Ref. [39]. Consequently,

these configurations represent two distinct cases of the model and hybrid star properties with the middle- and low-mass quark onset, and the maximum hybrid star mass exceeding that of the purely hadronic case and be-
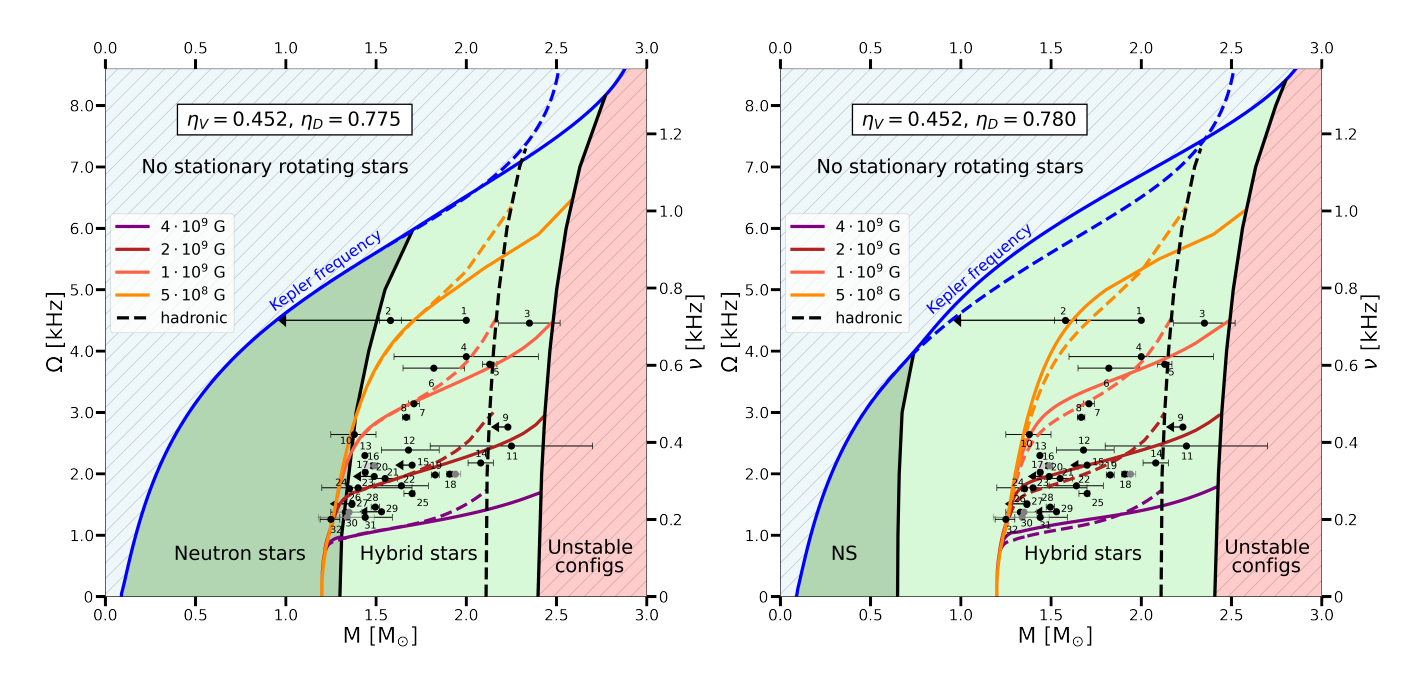
FIG. 8. The same as the upper panel of Fig. 7 but for different values of model parameters: $\eta_V = 0.452, \eta_D = 0.775$ (left panel) and $\eta_V = 0.452, \eta_D = 0.780$ (right panel). The dashed color lines cease to exist where the hadronic stars reach the instability limit (black dashed curve). The Kepler limit for the hadronic DD2npY-T EoS is depicted with the dashed blue curve.

ing below it.

Whether a star of a certain mass is a hybrid or a pure hadronic star is defined by the dense matter EoS. For the considered DD2npY-T – RDF hybrid EoS we map the star's configurations in Fig. 7 in the plane of the angular velocity as a function of the star's gravitational mass. By solving the hydrostatic equations for equilibrated stars with different spin frequencies, we depict the region where the stars are purely hadronic (the dark green area in Fig. 7), hybrid stars with a quark core (the light green area) as well as unstable configurations (the pink beige area) separated by the solid black curves. The latter refers to configurations exceeding the maximum gravitational mass, where stellar oscillations would cause the star to collapse into a black hole. The blue curve above corresponds to the mass-shedding limit. Moreover, Fig. 7 depicts the observational data on the fastest MSPs for which the mass measurements are available. The data are listed in Appendix B. The error bars represent a 1σ confidence interval, and for stars with only the upper estimate, the arrow indicates the range of masses. We observe that increasing the η_D value from 0.733 (left panel) to 0.743 (right panel) enlarges the hybrid star region, encompassing all depicted MSPs within their error bars. Interestingly, for $\eta_V = 0.3, \eta_D = 0.743$ all the rapidly rotating MSPs are predicted to be hybrid stars, while for $\eta_V = 0.3, \eta_D = 0.733$ only the stars above $\sim 1.5\ M_\odot$ are hybrid.

Compact stars born with a rapid rotation evolve by emitting electromagnetic radiation and gravitational waves, eventually losing their angular momentum. As the baryon number is conserved the evolutionary path goes along the constant rest mass M_0 line shown in the lower panels of Fig. 7. The color lines depict the evolutionary sequences (lines of NSs of constant rest mass, equal to baryon mass) as a function of the angular velocity Ω. The x-axis displays the gravitational mass. The black dashed curve represents the rotational limit defined by the onset of mass-shedding from the equator (the Kepler frequency), while the dotted and dash-dotted curves indicate the onset of the deconfinement phase transition and configurations unstable due to radial oscillations, respectively. The cyan and blue lines in the lower left panel, as well as the yellow and light green lines in the lower right panel of Fig. 7, illustrate the scenario where a hadronic star crosses the deconfinement onset as it spins down, further evolving as a hybrid star. In contrast, massive stars (represented by the red and brown lines) lack a static limit and will collapse into a black hole upon losing their angular velocity. Note that the evolutionary paths in the lower panels are obtained for unmagnetized non-accreting stars.

As you can see in Figs. 7-8 even the fastest-spinning pulsars, J1748+2446ad [10], 4U 1820–30 (J1820-30A) [71, 72], and J0952-0607 [9] are far from the Kepler limit (for the mass of J1748+2446ad there is only an upper limit, but it is unlikely that its mass is below $1M_\odot$). The fact of observing two of the fastest objects with very similar spin frequencies made us think that they corresponded to the cutoff limit. On the other hand, the MSPs depicted in Figs. 7-8 show clustering in the frequency (angular velocity) interval $210 \le f[Hz] \le 340$ ($1300 \le \Omega[Hz] \le 2140$). The question arises as to whether any physical mechanisms affect spin evolution, e.g., binary evolution,
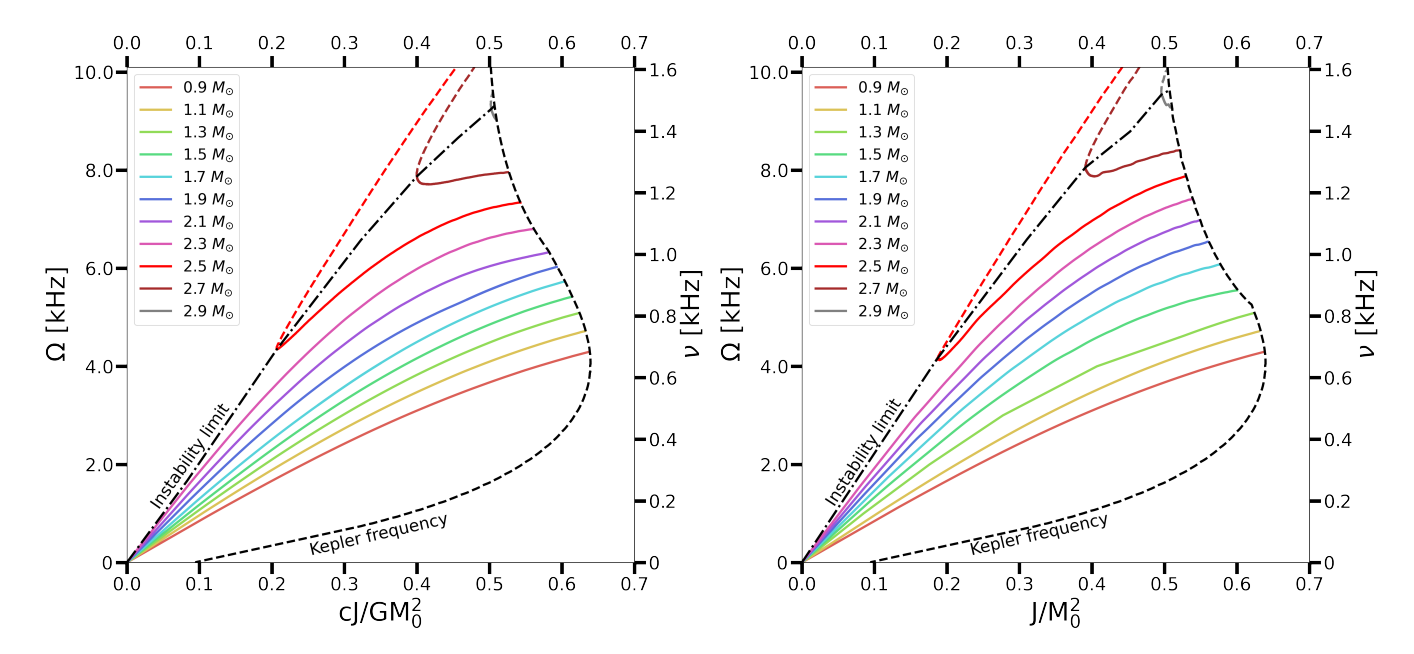
FIG. 9. The angular velocity Ω as a function of the angular momentum J divided by the rest mass squared for the fixed value of the vector coupling $\eta_V = 0.3$ and different values of the diquark coupling $\eta_D = 0.733$ (left panel) and $\eta_D = 0.743$ (right panel).

accretion, magnetic field evolution, the appearance of the exotic degrees of freedom in the star interior, etc.

A possible explanation for the population clustering caused by the waiting time in a certain frequency region is proposed by Poghosyan *et al.* [73]. The onset of quarks in the interior of rapidly rotating stars entails a characteristic change in the spin evolution. The star's spin evolution is defined by the strength of the magnetic field, accretion rate, and the appearance of quark matter. The evolutionary tracks for the $1.2M_\odot$ star with a fixed accretion rate of 10^{-7} $M_\odot yr^{-1}$, and initial magnetic field strength as indicated in the legend are shown in the upper panels of Fig. 7. The solid curves depict the hybrid EoSs, while the dashed curves are obtained for the hadronic DD2npY-T EoS. As shown, the curves reproduce the MSP data well and explain a pulsar clustering. For further details about the model, see Appendix C and Ref. [73].

Fig. 8 shows the modification of the angular velocity as a function of the gravitational mass for the model parameters $(\eta_V = 0.452, \eta_D = 0.775)$ and $(\eta_V = 0.452, \eta_D = 0.780)$ that resulted from the special point analysis of Ref. [39]. The value of $\eta_V = 0.452$ was fixed by the ω meson mass and determines the maximum mass limit (dashed black lines) while the range of admissible values for the diquark coupling, $\eta_D = 0.775$ and $\eta_D = 0.780$ determines the upper (left panel) and lower (right panel) limits for the onset of deconfinement, respectively. Compared to Fig. 7, the hybrid star regions in both panels are more extended, while the latter parameter set even encompasses all depicted MSPs.

Interestingly for these two pairs of η_V, η_D values, we see a big difference in the behaviors of the evolutionary

trajectories for the hybrid (solid) and hadronic (dashed) star of $1.2M_\odot$. The dashed curves cease to exist where the hadronic stars reach the instability limit (dotted lines), while the solid curves continue up to the instability limit. Notably, the black-widow pulsar J0952-0607 [9], labeled '3' in Fig. 8 can only be explained as a hybrid star with the favorable strong vector coupling $\eta_V = 0.452$, within the 1σ range of its mass because it lies beyond the limit of stability for the purely baryonic DD2npY-T EOS.

As was first classified by Cook *et al.* [17] the evolutionary sequences existing between the dashed and dashed-dotted black curves are the *normal* sequences that have a static limit (see the solid color lines in Fig. 9). For all pairs of couplings, the normal sequences of hybrid stars characterized by the constant rest mass values show a shift towards the higher gravitational mass near the Kepler frequency.

The second group of *supramassive* sequences does not have the static limit. Thus, the curves corresponding to the high rest mass values lack static or low-frequency counterparts. These stars while spinning down will collapse into black holes as the gravitational force becomes too strong, overcoming the repulsive forces.

The evolutionary behavior for normal and supramassive sequences is well presented in the plane of the angular velocity Ω as a function of the angular momentum J divided by the rest mass squared. The colorful dashed lines above the black dashed-dotted curve in Fig. 9 indicate the supramassive sequences. The solid color lines are the same as in Fig. 7 and obtained for the fixed values of the baryon mass.

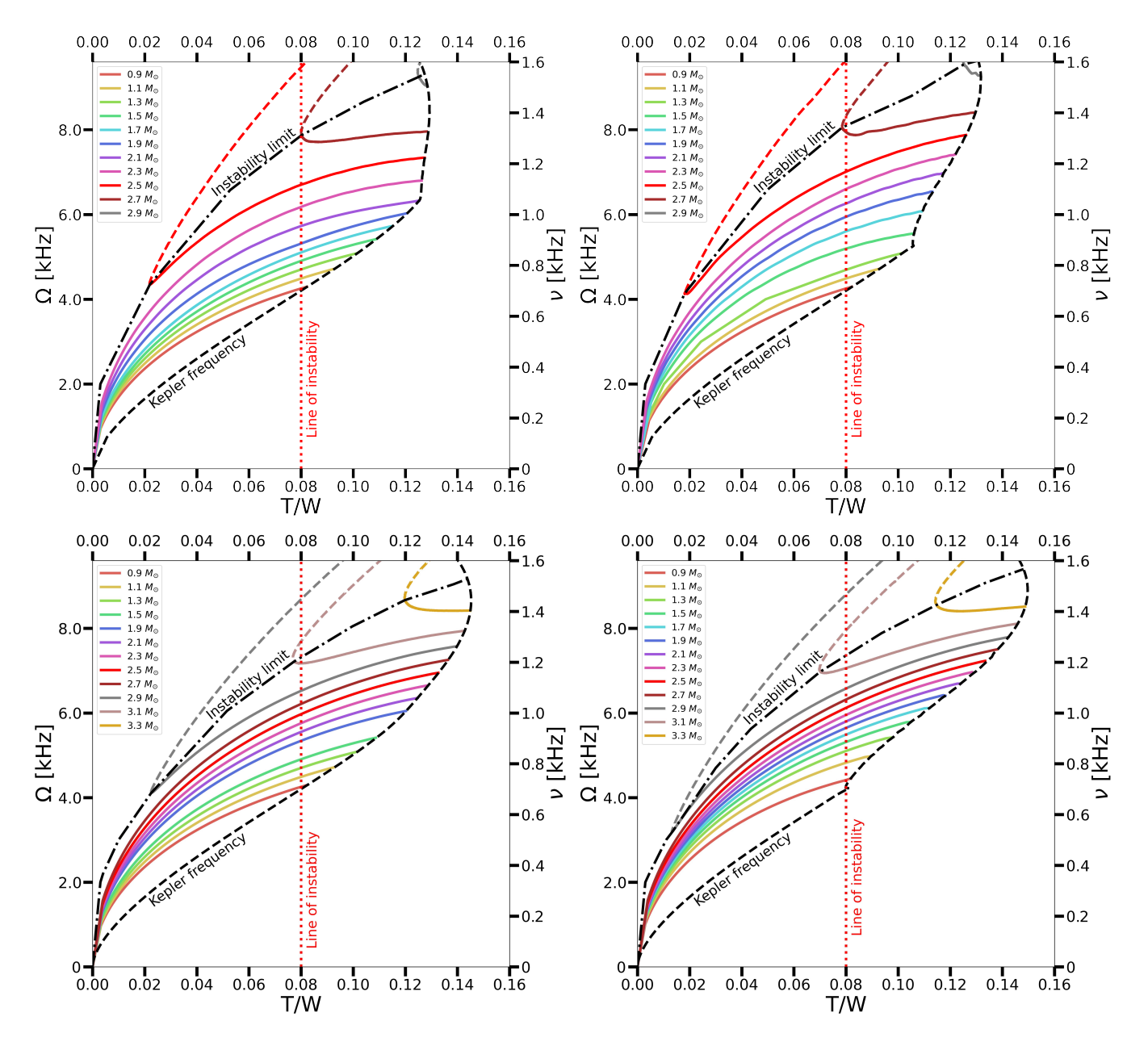For the normal NS sequences, the angular momentum

FIG. 10. The angular velocity as a function of the ratio of rotational kinetic T and gravitational potential W energy. **Upper panels:** the vector coupling is fixed to $\eta_V = 0.3$ and the diquark coupling equals $\eta_D = 0.733$ (left panel) and $\eta_D = 0.743$ (right panel). **Lower panels:** $\eta_V = 0.452$ and the diquark coupling $\eta_D = 0.775$ (left panel) and $\eta_D = 0.780$ (right panel). The colorful curves represent the constant rest mass values listed in the legend. The black dashed and dash-dotted curves depict the mass-shedding limit and collapse to a black hole, respectively. The red dotted line corresponds to the onset of axisymmetric instability mentioned in the text.

J consistently increases with Ω, indicating that along the normal sequence, stars do not spin up as the angular momentum decreases. The supramassive stars exhibit the opposite behavior; with angular momentum lost during evolution, the angular velocity increases. The stability condition for the star of constant rest mass M_0 is defined as $\frac{\partial J}{\partial \epsilon_c}|_{M_0} < 0$, where ϵ_c is the central energy density [17]. The onset point of the quasi-radial oscillations occurs at the lowest J value of each evolutionary sequence, i.e., on the dash-dotted curve dividing the two sequences. Fur-

thermore, by comparing the two panels in Fig. 9, we can conclude that for the higher value of the diquark coupling, the earlier onset makes hybrid stars more resistant to higher angular velocity and capable of sustaining a higher maximum mass.

A similar parameter, $K \equiv J/M^2$, where M is the gravitational mass of a star, is known as the Kerr parameter. This dimensionless spin parameter, which reaches its maximum value at the mass-shedding limit, indicates the star's proximity to collapse into a black hole. As
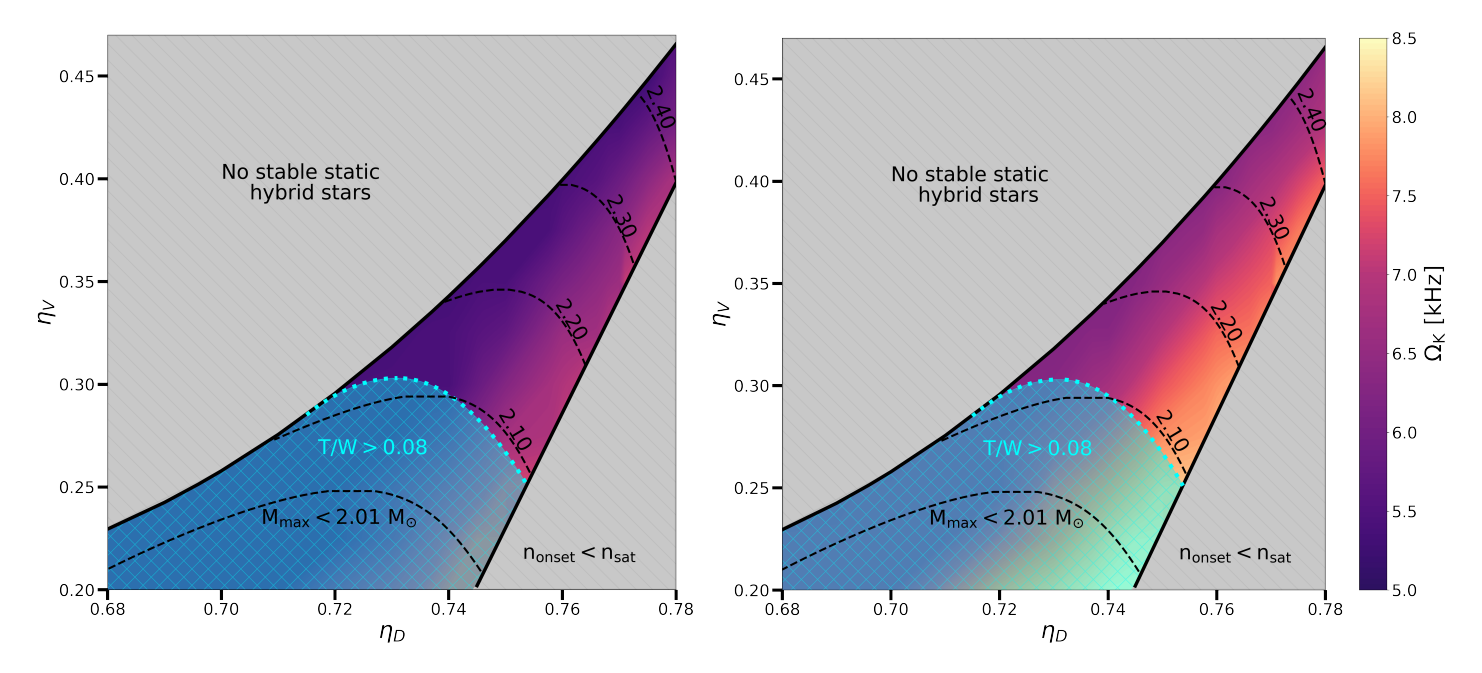
FIG. 11. Parameter space in the η_V - η_D plane calculated for the DD2npY-T - RDF hybrid EoS for the fixed value of the rest mass 1.5 $M_\odot$ (left panel) and 2.1 $M_\odot$ (right panel). The color represents the Kepler angular velocity of the rotating star in the region where the vector and diquark couplings are consistent with observational constraints on the maximum mass of NSs from [74]. The lavender region is excluded by the requirement of the stability of the quark branch and tidal deformability constraints from GW170817 [42] and GW190425 [43], while the light yellow region indicates the excluded region with the onset of the deconfinement phase transition below the saturation density. The dark green shaded area at the bottom corresponds to the excluded region of model parameters resulting in the maximum gravitational mass of the static stars below $M_{max} < 2.01 M_\odot$ [39]. The black dashed contour lines indicate the maximum achieved gravitational mass for those values of the parameters. The region excluded by the onset of gravitational radiation instabilities according to the criteria $T/W > 0.08$ for the Black Widow Pulsar J0952−0607 is displayed with the cyan hatched region.

shown in Ref. [75], a typical NS at the maximum mass reaches $K \sim 0.7$, while for a black hole, it equals 1.0.

Although the configurations between the mass-shedding limit (the dashed black curve) and instability limit causing stars to collapse into black holes (the dash-dotted black curve) are considered stable, the ratio of rotational and gravitational energy, T/W, is strongly related to the onset of the gravitational radiation-driven instability that causes the star collapse into the Kerr black hole [17, 48, 75]. In Fig. 10 the angular velocity Ω as the function of the T/W ratio is plotted for the sequence of hybrid stars of constant rest mass values (see solid curves of a different color). The vertical red dotted line indicates the onset of $l = m = 2$ f-mode instability at $T/W \simeq 0.08$ for the star of 1.4 $M_\odot$ gravitational mass [76]. Considering the weak dependence of the instability limit on the star's mass, we assume the same value for all stars is $T/W = 0.08$. In the Newtonian limit, the onset of the non-axisymmetric perturbations would set in at $T/W \simeq 0.14$ for the 1.4 $M_\odot$ star. For all four different sets of model parameter sets ($\eta_V = 0.3, \eta_D = 0.733$), ($\eta_V = 0.3, \eta_D = 0.743$), ($\eta_V = 0.452, \eta_D = 0.775$) and ($\eta_V = 0.452, \eta_D = 0.780$) the non-axisymmetric instabilities will arise before the Kepler frequency is reached. Moreover, the heaviest star configurations are entirely ruled out by this limit. Consequently, observing rapidly

rotating massive stars listed in Table III allows us to constrain the allowed values of η_V and η_D within the f-mode instability window.

Fig. 11 shows the allowed range of the model parameters in the η_V - η_D plane that are consistent with the existing NS observations. For the fixed value of the rest mass 1.5 $M_\odot$ (left panel) and 2.1 $M_\odot$ (right panel), the color represents the mass-shedding angular velocity together with the excluded range of model parameters that lead to unstable static hybrid stars, excluded by the tidal deformability constraints from GW170817 [42] and GW190425 [43], and the negative squared frequency of the fundamental mode of radial oscillations [57, 77] (see the shaded lavender region in Fig. 11). Note, the considered rest mass values 1.5 $M_\odot$ (left panel) and 2.1 $M_\odot$ (right panel) are equivalent to stars with the gravitational mass of $\sim 1.4 M_\odot$ and $\sim 1.9 M_\odot$, respectively. The gray region in the bottom right corner of both panels is excluded due to the criteria of the too early onset of the deconfinement phase transition. We require the phase transition to occur above the saturation density of normal nuclear matter, n_{sat}, equivalent to the onset mass $M_{onset} \geq 0.243 M_\odot$. Moreover, the excluded region of model parameters resulting in a maximum gravitational mass of static stars below $M_{max} < 2.01 M_\odot$, as found by Gärtlein et al. [39], is indicated by a labelled

dashed line at the bottom of both panels. The black dashed contour lines indicate the maximum gravitational mass of hybrid stars corresponding to those values of η_V, η_D. The cyan hatched region represents the limit for non-axisymmetric instabilities, determined by the criterion $T/W > 0.08$, derived for the Black Widow Pulsar J0952−0607 with a mass of 2.35 $M_\odot$ [9]. Particularly, the cyan hatched region depicts the excluded region where a star of 2.35 $M_\odot$ would have $T/W > 0.08$.

VI. CONCLUSIONS AND PERSPECTIVES

We have studied equilibrium configurations of rapidly rotating hybrid stars, focusing on how the phase transition between hadronic and quark matter within their interiors modifies the limits of stability at high spin frequencies. Our analysis was based on a hybrid EOS with a hadronic phase of hypernuclear matter and a color-superconducting quark matter phase described by a RDF approach. By systematically varying vector and diquark couplings in quark matter, we have explored the effects on the onset of the deconfinement and the maximum mass, ensuring consistency with astrophysical constraints, including the three NICER mass-radius measurements [32–36], and the tidal deformability measurements from the binary NS mergers GW170817 [42] and GW190425 [43].

A novel aspect of this study is the investigation of rotating hybrid stars undergoing an early deconfinement phase transition, along with its previously unexamined impact on the empirical relation between the Kepler frequency, gravitational mass, and radius of non-rotating NSs.

Our results demonstrate the significant impact of increasing rotational frequencies on key parameters of compact stars, including the gravitational mass, energy density profile, and angular momentum. We have illustrated how rotation affects the structure of hybrid stars, showing that the onset of the deconfinement phase transition shifts to higher masses as the spin frequency increases. This effect is particularly pronounced for configurations with late phase transitions, as evidenced by our analysis of different diquark coupling values. Moreover, we demonstrated that stars characterized by the higher values of the diquark coupling η_D can generally achieve higher rotation frequency or Kepler frequencies f_K, suggesting that more compact objects can sustain faster rotation.

A crucial aspect of our work is the revision of the empirical relation between the Kepler frequency, gravitational mass, and radius of non-rotating NSs. This relation was initially established under the assumption that all NSs, up to the heaviest, are either purely hadronic or quark stars. We proposed a parameterization for the C factor that accounts for various scenarios of deconfinement onset while reproducing the two limiting cases of purely hadronic and quark EoSs. The C factor is expressed as a function of the quark onset mass, $M_{\rm onset}$, in

the range between 0.5 $M_\odot$ and the maximum mass. By considering the currently fastest spinning pulsar, PSR J1748-2446ad, with its remarkable spin frequency of 716 Hz [10], we have revised a lower bound on the mass-radius relation of compact stars. The concept of minimum mass is as important as the upper limit providing the lowest stable star configurations. The lower limit is especially interesting in the context of the lightest HESS J1731-347 compact object [70, 78, 79]. Our analysis reveals how the deconfinement phase transition in an NS core modifies the lower limit on the mass and radius, consequently affecting the constraints on the dense matter EoS.

By analyzing the increase of the angular velocity as a function of the gravitational mass for hybrid stars with the different phase transition onset mass and quark matter properties governed by the η_V and η_D parameters we can map the region where the stars are hadronic or hybrid. These results are matched with observational data of the fastest-spinning MSPs with available mass measurements. We demonstrated the possibility of probing the interior composition of MSPs by tracing the evolutionary paths of unmagnetized stars with the same mass. We show that while spinning down with time, MSPs with hadronic matter in their interior could reach the conditions for the onset of the deconfinement phase transition and become hybrid stars. Similarly, fastly spinning heavy hybrid stars at their maximum mass limit could cease to exist due to reaching the instability line upon spinning down (see the red curve in the lower panel in Fig. 7).

Although the mass-shedding and the quasi-radial oscillation limits define the boundaries for stationary rotating stars to exist, we show that the stability condition against non-axisymmetric instabilities put an additional constraint narrowing down the region of admissible $\eta_V - \eta_D$ parameter values for hybrid star EOS. Particularly, the onset of the gravitational radiation-driven instability limits the higher frequencies for massive stars. The rotational and gravitational energy ratio $T/W \leq 0.08$ defines the stable configurations. Thus, the observation of the rapidly-rotating Black Widow Pulsar J0952−0607 with the gravitational mass of 2.35±0.17 $M_\odot$ [9] existing in the non-axisymmetric stability window provides a useful probe of the quark matter properties and the deconfinement onset, excluding $\eta_V \lesssim 0.27$. This limit yields a new constraint on the microphysical parameters of the model and quark matter properties, which has a big implication for the dense matter EoS.

As it is shown in Figs. 7 and 8, the fastest-rotating MSPs with the measured mass demonstrate a clear population clustering around 1.3-1.8$M_\odot$ and the frequency (angular velocity) of 210-340 Hz (1300-2140 Hz). Moreover, the detection of the two fastest spinning objects, i.e., J1748+2446ad and 4U 1820–30 (J1820-30A), with similar values of the spin frequency 716.36 Hz and 716 Hz, makes us think we might have approached the cut-off limit for NSs. Pulsar clustering and no pulsars found rotating faster than 716 Hz were suggested as a consequence of the deconfinement phase transition in the star

interior and magnetic field evolution [73]. On the upper panels of Figs. 7 and 8 we illustrate the spin evolution for the hybrid star of $1.2M_\odot$ for different values of the magnetic field that explains well the population clustering due to the waiting time in a certain frequency region and the spin frequency cut off. This upper limit is also supported by the Bayesian analysis of observable accretion- and nuclear-powered pulsars that give $f_{max} \sim 730$ Hz [71].

A striking result in favour of the hybrid NS case with color superconducting quark matter that we explored in this work is the fact that with the favoured parameter set we can describe the Black Widow Pulsar J0952-0607 with its high mass and spin, while this star is out of the 1σ range for an explanation by the purely hadronic EOS.

Looking ahead, the potential detection of a pulsar with a spin frequency of 1000 Hz or higher would be a game-changer. Such a discovery would enable robust discrimination between different EoS, significantly contributing to our understanding of NS interior composition and accretion. Our findings show that a pulsar with a spin frequency of 1000 Hz, would impose the upper limit $R_{1.4} \leq 11.90$ km considering the hybrid EoS and $R_{1.4} \leq 11.86$ km for the hadronic EoS. This underscores the importance of continued observational efforts and theoretical modeling in this field.

It is worth noting that out of over 3,000 known pulsars, 560 are classified as MSPs[2]. The field of pulsar astronomy is poised for significant advancements with upcoming and ongoing radio surveys. Initiatives such as the Five-hundred-meter Aperture Spherical radio Telescope (FAST) [80], MeerKAT [81], and the Square Kilometre Array (SKA) [82], are expected to substantially increase the number of detected pulsars. These surveys promise to provide crucial data on pulsar masses and frequencies, which will be instrumental in further constraining the EoS of strongly interacting matter.

On the other hand, future X-ray telescopes such as Advanced Telescope for High ENergy Astrophysics (Athena) [83], STROBE-X [84], and enhanced X-ray Timing and Polarimetry (eXTP) [85] should be able to provide mass and radius measurement for even fainter pulsars.

Our study also highlights the complexity of modeling rapidly rotating compact stars. The framework we have employed, based on the RNS code [48], allows for the accurate calculation of stellar properties in the presence of strong gravitational fields and rapid rotation. This approach is instrumental in understanding the behavior of MSPs and their implications for fundamental physics.

In conclusion, our study underscores the importance of considering rotation and phase transitions in modeling compact stars. The interplay between these factors significantly influences our interpretation of observational data and understanding of the extreme state of matter

within NSs. As we await more precise measurements from future surveys, the field of NS physics remains a vibrant area of research.

Appendix A: ABPR parametrization of the RDF EOS

We present the effective number of degrees of freedom, pairing gap, and bag constant of the ABPR parameterization of the RDF EoS from Ref. [45]

$$A_4 = a_1 + b_1\eta_V + c_1\eta_V^2 + \left(d_1 + \frac{e_1}{\eta_V}\right)\eta_D, \quad \text{(A1)}$$

$$\Delta = (a_2 + b_2\eta_V + c_2\eta_V^2)\sqrt{d_2 + e_2\eta_V + \eta_D}, \quad \text{(A2)}$$

$$B = a_3 + b_3\eta_V + c_3\eta_V^2 + d_3\eta_D + e_3\eta_D^2. \quad \text{(A3)}$$

The 15 parameters a_i, b_i, c_i, d_i, e_i with $i = 1, 2, 3$ were extracted from the fit of the original RDF EoS. Their values are presented in Table II. For more details about the fit see [39].

Appendix B: Parameters of millisecond pulsars with known masses

Table III includes observational data of the fastest spinning MSPs, with spin frequency f>200 Hz, for which

---

i	units	a_i	b_i	c_i	d_i	e_i
1	[ ]	0.757	-1.955	1.799	-0.063	0.046
2	[MeV]	300.7	8.534	-308.2	-0.235	1.458
3	[MeV/fm^3]	72.018	170.8	-241.0	512.7	-626.6

TABLE II. Values of the parameters of Eqs. (A1-A3).

the mass measurements are available. The pulsars are shown in Figs. 7-8. Number 2 corresponds to the recently reported observation by the NICER telescope of the second fastest spinning pulsar 4U 1820–30 (J1820−30A) with 716 Hz frequency [71]. For objects with several independent measurements, i.e., points 16,18,30,31, we plot them with a gray color.

Appendix C: Spin evolution by mass accretion

We present the underlying model for the evolutionary path of accreting and magnetized MSPs based on [73].

The differential equation we solve is given by

$$\frac{d\Omega}{dt} = \frac{K_{\text{ext}} - K_{\text{int}}}{I(\Omega, N) + \Omega(\partial I(N,\Omega)/\partial\Omega)_N}. \quad \text{(C1)}$$

The evolution of the angular velocity of a star depends on the external and internal torque, K_{ext} and K_{int}, the accretion rate, and the decay of the magnetic field. The considered expression for the exponential decay of the magnetic field of the accretors and the time dependence of the baryon number for the constant accreting rate $\dot{N}$ are given by

$$B(t) = [B(0) - B_\infty]\exp(-t/\tau_B) + B_\infty, \quad \text{(C2)}$$
$$N(t) = N(0) + t\dot{N}, \quad \text{(C3)}$$

where $N(0)$ and $B(0)$ denote the baryon number initial values and the magnetic field strength, respectively. τ_B is the typical decay time of the magnetic field. The remnant magnetic field is chosen to be $B_\infty = 10^8$ G. Additionally, the dependence on the EoS enters through the moment of inertia and its derivatives with respect to N and Ω. These terms enter the equation in the K_{int} as well as the denominator. For more details about the model see Ref. [73].

[1] D. Bhattacharya and E. P. J. van den Heuvel, Phys. Rep. **203**, 1 (1991).
[2] R. Wijnands and M. van der Klis, Nature **394**, 344 (1998).
[3] S. Guillot et al., Astrophys. J. Lett. **887**, L27 (2019), arXiv:1912.05708 [astro-ph.HE].
[4] M. Kramer et al., Science **314**, 97 (2006), arXiv:astro-ph/0609417.
[5] M. Bejger, T. Bulik, and P. Haensel, Mon. Not. Roy. Astron. Soc. **364**, 635 (2005), arXiv:astro-ph/0508105.
[6] M. Kramer and N. Wex, Class. Quant. Grav. **26**, 073001 (2009).
[7] G. Raaijmakers et al., Astrophys. J. Lett. **887**, L22 (2019), arXiv:1912.05703 [astro-ph.HE].
[8] R. W. Romani, D. Kandel, A. V. Filippenko, T. G. Brink, and W. Zheng, Astrophys. J. Lett. **908**, L46 (2021), arXiv:2101.09822 [astro-ph.HE].
[9] R. W. Romani, D. Kandel, A. V. Filippenko, T. G. Brink, and W. Zheng, Astrophys. J. Lett. **934**, L17 (2022), arXiv:2207.05124 [astro-ph.HE].
[10] J. W. T. Hessels, S. M. Ransom, I. H. Stairs, P. C. C. Freire, V. M. Kaspi, and F. Camilo, Science **311**, 1901 (2006), arXiv:astro-ph/0601337.
[11] B. Haskell, J. L. Zdunik, M. Fortin, M. Bejger, R. Wijnands, and A. Patruno, Astron. Astrophys. **620**, A69 (2018), arXiv:1805.11277 [astro-ph.HE].
[12] A. Patruno, B. Haskell, and N. Andersson, Astrophys. J. **850**, 106 (2017), arXiv:1705.07669 [astro-ph.HE].
[13] N. K. Glendenning and F. Weber, Astrophys. J. Lett. **559**, L119 (2001), arXiv:astro-ph/0003426.
[14] M. Bejger, D. Blaschke, P. Haensel, J. L. Zdunik, and M. Fortin, Astron. Astrophys. **600**, A39 (2017), arXiv:1608.07049 [astro-ph.HE].
[15] J. L. Friedman, L. Parker, and J. R. Ipser, Astrophys. J. **304**, 115 (1986).
[16] H. Komatsu, Y. Eriguchi, and I. Hachisu, Mon. Not. Roy. Astron. Soc. **237**, 355 (1989).
[17] G. B. Cook, S. L. Shapiro, and S. A. Teukolsky, Astrophys. J. **422**, 227 (1994).
[18] G. B. Cook, S. L. Shapiro, and S. A. Teukolsky, Astrophys. J. **424**, 823 (1994).
[19] N. Stergioulas and J. L. Friedman, Astrophys. J. **444**, 306 (1995), arXiv:astro-ph/9411032.
[20] C. J. Krüger, K. D. Kokkotas, P. Manoharan, and S. H. Völkel, Front. Astron. Space Sci. **8**, 736918 (2021), arXiv:2110.00393 [gr-qc].
[21] F. Weber, M. Orsaria, and R. Negreiros, in Compact Stars in the QCD Phase Diagram III (2013) arXiv:1307.1103 [astro-ph.SR].
[22] M. V. Beznogov, J. Novak, D. Page, and A. R. Raduta, Astrophys. J. **942**, 72 (2023), arXiv:2206.04539 [astro-ph.HE].
[23] P. G. Krastev, B.-A. Li, and A. Worley, Astrophys. J. **676**, 1170 (2008), arXiv:0709.3621 [astro-ph].
[24] J. L. Zdunik, M. Bejger, P. Haensel, and E. Gourgoulhon, Astron. Astrophys. **450**, 747 (2006), arXiv:astro-ph/0509806.
[25] H. Dimmelmeier, M. Bejger, P. Haensel, and J. L. Zdunik, Mon. Not. Roy. Astron. Soc. **396**, 2269 (2009), arXiv:0901.3819 [astro-ph.SR].
[26] N. Ippolito, M. Ruggieri, D. Rischke, A. Sedrakian, and F. Weber, Phys. Rev. D **77**, 023004 (2008), arXiv:0710.3874 [astro-ph].

Number	Name	f [Hz]	$M/M_\odot$	Ref.
1	J1748+2446ad	716.36	<2	[10]
2	J1820−30A	716.00	1.58±0.06	[71, 72]
3	J0952−0607	709.21	2.35±0.17	[9]
4	B1957+20	622.15	1.81±0.07	[86]
5	J1810+1744	602.41	2.13±0.04	[8]
6	J1023+0038	592.42	1.82±0.17	[87]
7	J0955−6150	500.160	1.71±0.03	[88]
8	J1903+0327	465.135	1.667±0.021	[89]
9	J1748−2446ao	439.681	<2.23	[90]
10	J2043+1711	420.189	$1.38^{+0.12}_{-0.13}$	[91]
11	J1311+3430	390.57	1.8–2.7	[92]
12	J1125−6014	380.173	$1.68^{+0.17}_{-0.15}$	[93]
13	J0337+1715	365.95	1.4378±0.0013	[94]
14	J0740+6620	346.532	2.08±0.07	[74]
15	J1748−2446am	340.853	<1.7	[95]
16	J1909−3744	339.316	1.48±0.03	[91]
			1.492±0.014	[96]
			1.45±0.03	[93]
17	J1012−4235	322.462	$1.44^{+0.013}_{-0.012}$	[97]
18	J1614−2230	317.379	1.908±0.016	[91]
			1.94±0.03	[93]
19	J1946+3417	315.444	1.828±0.022	[98]
20	J0024−7204H	311.493	<1.49	[99]
21	J1910−5958A	306.167	1.55±0.07	[100]
22	J0751+1807	287.458	1.64±0.15	[101]
23	J1933−6211	282.212	$1.4^{+0.3}_{-0.2}$	[102]
24	J2234+0611	279.597	$1.353^{+0.014}_{-0.017}$	[103]
25	J1748−2446ap	267.044	$1.700^{+0.015}_{-0.045}$	[90]
26	J1824−2452C	240.484	<1.367	[104]
27	J1807−2500B	238.881	1.3655±0.0021	[105]
28	J1950+2414	232.300	1.496±0.023	[106]
29	J1748−2446au	219.866	<1.53	[90]
30	J1713+0747	218.811	$1.33^{+0.09}_{-0.08}$	[101]
			1.35±0.07	[91]
31	J0030+0451	205.53	$1.44^{+0.15}_{-0.14}$	[32]
			$1.34^{+0.15}_{-0.16}$	[33]
32	J0514−4002A	200.378	$1.25^{+0.05}_{-0.06}$	[107]

TABLE III. Data of the fastest MSPs with spin frequency f>200 Hz and available mass measurements. The columns include the pulsar's number in Figs. 7-8, the number in the catalog, spin frequency, gravitational mass, and the corresponding references. All mass measurements are listed within one standard deviation, while the J1903+0327 observed data are listed within three standard deviations.

[27] S. K. Dhiman, G. Mahajan, and B. K. Agrawal, Nucl. Phys. A **836**, 183 (2010).

[28] N. S. Ayvazyan, G. Colucci, D. H. Rischke, and A. Sedrakian, Astron. Astrophys. **559**, A118 (2013), arXiv:1308.3053 [astro-ph.SR].

[29] S. Bhattacharyya, I. Bombaci, D. Bandyopadhyay, A. V. Thampan, and D. Logoteta, New Astron. **54**, 61 (2017), arXiv:1701.03489 [astro-ph.HE].

[30] N. K. Largani, T. Fischer, A. Sedrakian, M. Cierniak, D. E. Alvarez-Castillo, and D. B. Blaschke, Mon. Not. Roy. Astron. Soc. **515**, 3539 (2022), arXiv:2112.10439 [astro-ph.HE].

[31] S. L. Shapiro and S. A. Teukolsky, *Black holes, white dwarfs, and neutron stars: The physics of compact ob-jects* (1983).

[32] M. C. Miller *et al.*, Astrophys. J. Lett. **887**, L24 (2019), arXiv:1912.05705 [astro-ph.HE].

[33] T. E. Riley *et al.*, Astrophys. J. Lett. **887**, L21 (2019), arXiv:1912.05702 [astro-ph.HE].

[34] M. C. Miller *et al.*, Astrophys. J. Lett. **918**, L28 (2021), arXiv:2105.06979 [astro-ph.HE].

[35] T. E. Riley *et al.*, Astrophys. J. Lett. **918**, L27 (2021), arXiv:2105.06980 [astro-ph.HE].

[36] D. Choudhury *et al.*, (2024), arXiv:2407.06789 [astro-ph.HE].

[37] J. Antoniadis *et al.*, Science **340**, 6131 (2013), arXiv:1304.6875 [astro-ph.HE].

[38] O. Ivanytskyi and D. Blaschke, Phys. Rev. D **105**, 114042 (2022), arXiv:2204.03611 [nucl-th].

[39] C. Gärtlein, O. Ivanytskyi, V. Sagun, and D. Blaschke, Phys. Rev. D **108**, 114028 (2023), arXiv:2301.10765 [nucl-th].

[40] M. Alford, M. Braby, M. W. Paris, and S. Reddy, Astrophys. J. **629**, 969 (2005), arXiv:nucl-th/0411016.

[41] M. Shahrbaf, D. Blaschke, S. Typel, G. R. Farrar, and D. E. Alvarez-Castillo, Phys. Rev. D **105**, 103005 (2022), arXiv:2202.00652 [nucl-th].

[42] B. P. Abbott *et al.* (LIGO Scientific, Virgo), Phys. Rev. Lett. **121**, 161101 (2018), arXiv:1805.11581 [gr-qc].

[43] B. P. Abbott *et al.* (LIGO Scientific, Virgo), Astrophys. J. Lett. **892**, L3 (2020), arXiv:2001.01761 [astro-ph.HE].

[44] S. Typel, J. Phys. G **45**, 114001 (2018).

[45] O. Ivanytskyi and D. B. Blaschke, Particles **5**, 514 (2022), arXiv:2209.02050 [nucl-th].

[46] F. Cipolletta, C. Cherubini, S. Filippi, J. Rueda, and R. Ruffini, Physical Review D **92** (2015), 10.1103/physrevd.92.023007.

[47] C. Chakraborty, K. P. Modak, and D. Bandyopadhyay, Astrophys. J. **790**, 2 (2014), arXiv:1402.6108 [astro-ph.HE].

[48] V. Paschalidis and N. Stergioulas, Living Rev. Rel. **20**, 7 (2017), arXiv:1612.03050 [astro-ph.HE].

[49] E. Poisson and J. Doucot, Phys. Rev. D **95**, 044023 (2017), arXiv:1612.04255 [gr-qc].

[50] J. M. Baarden, in *Les Houches Summer School of Theoretical Physics: Black Holes* (1973) pp. 241–290.

[51] R. C. Tolman, Phys. Rev. **55**, 364 (1939).

[52] J. R. Oppenheimer and G. M. Volkoff, Phys. Rev. **55**, 374 (1939).

[53] N. Stergioulas, Living Rev. Rel. **1**, 8 (1998), arXiv:gr-qc/9805012.

[54] M. Cierniak and D. Blaschke, Eur. Phys. J. ST **229**, 3663 (2020), arXiv:2009.12353 [astro-ph.HE].

[55] B. K. Harrison, K. S. Thorne, M. Wakano, and J. A. Wheeler, "Gravitation theory and gravitational collapse," (1965).

[56] E. Gourgoulhon, P. Haensel, and D. Gondek, Astron. Astrophys. **294**, 747 (1995).

[57] V. Sagun, G. Panotopoulos, and I. Lopes, Phys. Rev. D **101**, 063025 (2020), arXiv:2002.12209 [astro-ph.HE].

[58] D. M. Sedrakyan and E. V. Chubaryan, Astrophysics **4**, 87 (1968).

[59] D. M. Sedrakyan and E. V. Chubaryan, Astrophysics **4**, 227 (1968).

[60] E. Chubarian, H. Grigorian, G. S. Poghosyan, and D. Blaschke, Astron. Astrophys. **357**, 968 (2000), arXiv:astro-ph/9903489.

[61] A. Konstantinou and S. M. Morsink, Astrophys. J. **934**, 139 (2022), arXiv:2206.12515 [astro-ph.HE].

[62] J. B. Hartle, Astrophys. J. **150**, 1005 (1967).

[63] J. B. Hartle and K. S. Thorne, Astrophys. J. **153**, 807 (1968).

[64] S. L. Shapiro, S. A. Teukolsky, and I. Wasserman, Astroph. J. **272**, 702 (1983).

[65] S. L. Shapiro, S. A. Teukolsky, and I. Wasserman, Nature **340**, 451 (1989).

[66] P. Haensel, J. L. Zdunik, M. Bejger, and J. M. Lattimer, Astron. Astrophys. **502**, 605 (2009), arXiv:0901.1268 [astro-ph.SR].

[67] J. M. Lattimer and M. Prakash, Science **304**, 536 (2004), arXiv:astro-ph/0405262.

[68] R. Riahi, S. Z. Kalantari, and J. A. Rueda Hernandez, Phys. Rev. D **99**, 043004 (2019), arXiv:1902.00349 [astro-ph.HE].

[69] C. Breu and L. Rezzolla, Mon. Not. Roy. Astron. Soc. **459**, 646 (2016), arXiv:1601.06083 [gr-qc].

[70] V. Doroshenko, V. Suleimanov, G. Pühlhofer, and et al., Nature Astronomy **6**, 1444 (2022).

[71] G. K. Jaisawal, Z. F. Bostancım, T. Boztepe, T. Güver, T. E. Strohmayer, D. R. Ballantyne, J. H. Beck, E. Göğüş, D. Altamirano, Z. Arzoumanian, D. Chakrabarty, K. C. Gendreau, S. Guillot, R. M. Ludlam, M. Ng, A. Sanna, and J. Chenevez, Astrophys. J. **975**, 67 (2024).

[72] T. Guver, P. Wroblewski, L. Camarota, and F. Ozel, Astrophys. J. **719**, 1807 (2010), arXiv:1002.3825 [astro-ph.HE].

[73] G. S. Poghosyan, H. Grigorian, and D. Blaschke, Astrophys. J. Lett. **551**, L73 (2001), arXiv:astro-ph/0101002.

[74] E. Fonseca et al., Astrophys. J. Lett. **915**, L12 (2021), arXiv:2104.00880 [astro-ph.HE].

[75] P. S. Koliogiannis and C. C. Moustakidis, Astrophys. J. **912**, 69 (2021), arXiv:2007.10424 [astro-ph.HE].

[76] S. M. Morsink, N. Stergioulas, and S. R. Blattnig, Astrophys. J. **510**, 854 (1999), arXiv:gr-qc/9806008.

[77] F. Di Clemente, M. Mannarelli, and F. Tonelli, Phys. Rev. D **101**, 103003 (2020), arXiv:2002.09483 [gr-qc].

[78] Y. Suwa, T. Yoshida, M. Shibata, H. Umeda, and K. Takahashi, Mon. Not. Roy. Astron. Soc. **481**, 3305 (2018), arXiv:1808.02328 [astro-ph.HE].

[79] V. Sagun, E. Giangrandi, T. Dietrich, O. Ivanytskyi, R. Negreiros, and C. Providência, Astrophys. J. **958**, 49 (2023), arXiv:2306.12326 [astro-ph.HE].

[80] R. Nan, D. Li, C. Jin, Q. Wang, L. Zhu, W. Zhu, H. Zhang, Y. Yue, and L. Qian, Int. J. Mod. Phys. D **20**, 989 (2011), arXiv:1105.3794 [astro-ph.IM].

[81] P. V. Padmanabh et al., (2023), 10.1093/mnras/stad1900, arXiv:2303.09231 [astro-ph.HE].

[82] A. Watts et al., PoS **AASKA14**, 043 (2015), arXiv:1501.00042 [astro-ph.SR].

[83] X. Barcons et al., (2012), arXiv:1207.2745 [astro-ph.HE].

[84] P. S. Ray et al. (STROBE-X Science Working Group), (2019), arXiv:1903.03035 [astro-ph.IM].

[85] S.-N. Zhang et al. (eXTP), Sci. China Phys. Mech. Astron. **62**, 29502 (2019), arXiv:1812.04020 [astro-ph.IM].

[86] C. J. Clark et al., Nature Astron. **7**, 451 (2023), arXiv:2301.10995 [astro-ph.HE].

[87] J. Strader et al., Astrophys. J. **872**, 42 (2019), arXiv:1812.04626 [astro-ph.HE].

[88] M. Serylak et al., Astron. Astrophys. **665**, A53 (2022), arXiv:2203.00607 [astro-ph.HE].

[89] P. C. C. Freire et al., Mon. Not. Roy. Astron. Soc. **412**, 2763 (2011), arXiv:1011.5809 [astro-ph.GA].

[90] P. V. Padmanabh et al., Astron. Astrophys. **686**, A166 (2024), arXiv:2403.17799 [astro-ph.HE].

[91] Z. Arzoumanian et al. (NANOGrav), Astrophys. J. Suppl. **235**, 37 (2018), arXiv:1801.01837 [astro-ph.HE].

[92] R. W. Romani, A. V. Filippenko, and S. B. Cenko, Astrophys. J. **804**, 115 (2015), arXiv:1503.05247 [astro-ph.HE].

[93] M. Shamohammadi et al., Mon. Not. Roy. Astron. Soc. **520**, 1789 (2023), arXiv:2212.04051 [astro-ph.HE].

[94] S. M. Ransom et al., Nature **505**, 520 (2014), arXiv:1401.0535 [astro-ph.SR].

[95] B. C. Andersen and S. M. Ransom, Astrophys. J. Lett. **863**, L13 (2018), arXiv:1807.07900 [astro-ph.HE].

[96] K. Liu et al., Mon. Not. Roy. Astron. Soc. **499**, 2276 (2020), arXiv:2009.12544 [astro-ph.HE].

[97] T. Gautam, P. C. C. Freire, J. Wu, V. Venkatraman Krishnan, M. Kramer, E. D. Barr, M. Bailes, and A. D. Cameron, Astron. Astrophys. **682**, A103 (2024), arXiv:2311.13563 [astro-ph.HE].

[98] E. D. Barr, P. C. C. Freire, M. Kramer, D. J. Champion, M. Berezina, C. G. Bassa, A. G. Lyne, and B. W. Stappers, Mon. Not. Roy. Astron. Soc. **465**, 1711 (2017), arXiv:1611.03658 [astro-ph.HE].

[99] P. C. C. Freire et al., Mon. Not. Roy. Astron. Soc. **471**, 857 (2017), arXiv:1706.04908 [astro-ph.HE].

[100] A. Corongiu et al., Astron. Astrophys. **671**, A72 (2023), arXiv:2301.04055 [astro-ph.HE].

[101] G. Desvignes et al. (EPTA), Mon. Not. Roy. Astron. Soc. **458**, 3341 (2016), arXiv:1602.08511 [astro-ph.HE].

[102] M. Geyer et al., Astron. Astrophys. **674**, A169 (2023), arXiv:2304.09060 [astro-ph.HE].

[103] K. Stovall et al., Astrophys. J. **870**, 74 (2019), arXiv:1809.05064 [astro-ph.HE].

[104] S. Begin, A search for fast pulsars in globular clusters, Ph.D. thesis, University of British Columbia (2006).

[105] R. S. Lynch, P. C. C. Freire, S. M. Ransom, and B. A. Jacoby, Astrophys. J. **745**, 109 (2012), arXiv:1112.2612 [astro-ph.HE].

[106] W. W. Zhu et al., Astrophys. J. **881**, 165 (2019), arXiv:1907.05046 [astro-ph.SR].

[107] A. Ridolfi, P. C. C. Freire, Y. Gupta, and S. M. Ransom, Mon. Not. Roy. Astron. Soc. **490**, 3860 (2019), arXiv:1909.06163 [astro-ph.HE].